


# Quantum-optical influences in optoelectronics—An introduction

Cite as: Appl. Phys. Rev. 5, 041302 (2018); <https://doi.org/10.1063/1.5045580>

Submitted: 21 June 2018 . Accepted: 19 September 2018 . Published Online: 26 October 2018

Weng W. Chow, and Stephan Reitzenstein 

## COLLECTIONS

 This paper was selected as Featured



View Online



Export Citation



CrossMark

## ARTICLES YOU MAY BE INTERESTED IN

[Materials for optical fiber lasers: A review](#)

Applied Physics Reviews 5, 041301 (2018); <https://doi.org/10.1063/1.5048410>

[Recent advances in Wigner function approaches](#)

Applied Physics Reviews 5, 041104 (2018); <https://doi.org/10.1063/1.5046663>

[Graphene and related two-dimensional materials: Structure–property relationships for electronics and optoelectronics](#)

Applied Physics Reviews 4, 021306 (2017); <https://doi.org/10.1063/1.4983646>



Applied Physics Reviews

Submit your original research today!

LEARN MORE >>>

Journal  
Impact Factor  
**12.750**

AIP  
Publishing

## Quantum-optical influences in optoelectronics—An introduction

Weng W. Chow<sup>1</sup> and Stephan Reitzenstein<sup>2</sup>

<sup>1</sup>Sandia National Laboratories, Albuquerque, New Mexico 87185-1086, USA

<sup>2</sup>Institut für Festkörperphysik, Technische Universität Berlin, 10623 Berlin, Germany

(Received 21 June 2018; accepted 19 September 2018; published online 26 October 2018)

This focused review discusses the increasing importance of quantum optics in the physics and engineering of optoelectronic components. Two influences relating to cavity quantum electrodynamics are presented. One involves the development of low threshold lasers, when the channeling of spontaneous emission into the lasing mode becomes so efficient that the concept of lasing needs revisiting. The second involves the quieting of photon statistics to produce single-photon sources for applications such as quantum information processing. An experimental platform, consisting of quantum-dot gain media inside micro- and nanocavities, is used to illustrate these influences of the quantum mechanical aspect of radiation. An overview is also given on cavity quantum electrodynamics models that may be applied to analyze experiments or design devices. *Published by AIP Publishing.* <https://doi.org/10.1063/1.5045580>

### TABLE OF CONTENTS

I. INTRODUCTION .....	1
II. REVISITING LASER PHYSICS.....	2
A. Towards smaller lasers.....	2
B. Channeling spontaneous emission .....	3
C. High- $\beta$ lasing.....	3
D. Lasing and the intracavity photon number ..	4
III. QUIETING PHOTON STATISTICS.....	5
A. Types of light .....	5
B. Single-photon generation.....	6
1. Cavity enhancement .....	6
2. Single-quantum-dot devices.....	6
3. Emission rate versus purity .....	8
IV. MODELING QUANTUM OPTICAL EFFECTS.....	10
A. Hamiltonian and cluster expansion .....	10
B. Levels of detail and comparison.....	11
1. Basic model .....	11
2. Reduction to 2-rate equation limit .....	12
3. QD-QW model.....	12
4. Comparison.....	13
C. Caution: Underestimating $\beta$ .....	13
1. QD inhomogeneous broadening .....	13
2. Inter-QD correlations .....	15
3. Quantum-confined Stark effect .....	16
V. SUMMARY AND OUTLOOK .....	17
A. Scope.....	17
B. Progression from physics to devices .....	17
C. To the physicist.....	17
D. To the engineer.....	18

### I. INTRODUCTION

Optoelectronics is entering an exciting period. There are intense device development activities driven by applications

ranging from telecommunications and room lighting to the internet and quantum information processing. Significant advances are being made in laser performance, including reducing spatial footprint, consuming and emitting less energy, improving spectral stability, and controlling photon statistics. Common to these activities is the increasing role of quantum optics. The importance of contributions due to the quantum mechanical aspect of radiation is evident when analyzing experiments and enabling new functionalities. While the underlying physics has been established long ago, its implementation to develop components that are a short step from being applicable in optoelectronics represents forefront applied physics and engineering.

Our goal in this focused review is to introduce the reader to how quantum optics, as originally developed for atomic, molecular, and optical (AMO) systems, is being extended for use in semiconductor device research. (For textbook descriptions of AMO quantum optics and semiconductor device engineering, see Refs. 1 and 2, respectively.) It is a growing effort, with important contributions from many groups throughout the world. We hope to give the general audience a flavor of the common interests and challenges, as well as a background understanding for further learning from recent literature covering both science and engineering aspects.

Quantum optics enters optoelectronics in diverse ways. It is used to develop new properties to enable new applications. Other times, it is necessary to explain behaviors in devices we are trying to improve, especially for devices performing close to fundamental limits. This review will illustrate these two functions with examples from cavity quantum electrodynamics (CQED) research involving quantum-dot (QD) micro- or nanocavity light sources.

A QD, micro- or nanocavity light source (see, e.g., Fig. 1) is a good experimental platform for studying laser physics and exploring device applications. Section II describes new

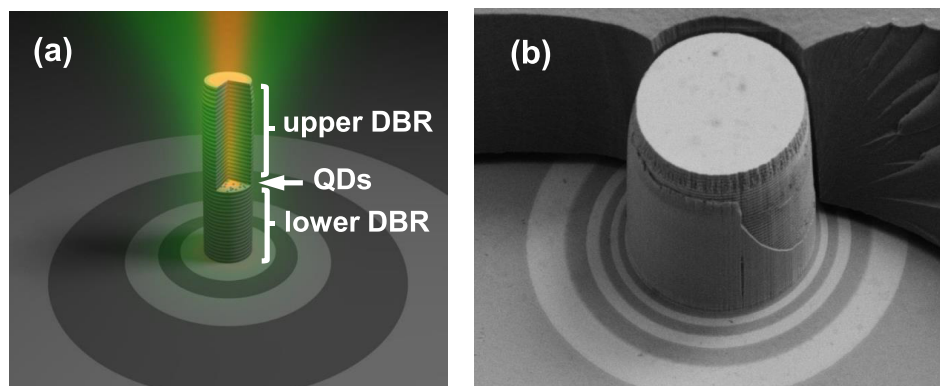


FIG. 1. (a) Sketch showing the basic features of a QD, high- $\beta$  emitter. In our investigations, we considered a micro- or nano-pillar optical cavity defined by a pair of distributed Bragg reflectors (DBRs) sandwiching a QD gain region. (b) Scanning electron microscopy (SEM) image of an actual  $8\ \mu\text{m}$  diameter micro-pillar fabricated using electron-beam lithography and plasma reactive ion etching. Part of the planarizing BCB polymer layer was mechanically removed to show the free-standing pillar. While the shown device is optically pumped, lasing with current injection has been demonstrated in recent structures. Reprinted with permission from S. Kreinberg *et al.*, *Light: Sci. Appl.* **6**, e17030 (2017). Copyright 2017 Nature Publishing Group.<sup>3</sup>

questions involving lasing when the channeling of spontaneous emission into a single or very few cavity modes becomes very efficient. This has been demonstrated with the class of micro- and nanocavities, referred to as high-spontaneous-emission (or high- $\beta$ ) cavities. For lasers using these high- $\beta$  cavities, the transition from spontaneous emission to lasing is distinctly different from that of conventional (low- $\beta$ ) lasers. The use of CQED to explain observed new behaviors is demonstrated. Section III describes an example of new functionality in semiconductor light sources arising from emphasizing the quantum optics aspect of active regions, made possible by the maturing of semiconductor QDs. The high optical gain per active material volume enables light-source operation with very few QDs. This gives rise to a possibility of producing nonclassical light, which exhibit photon number fluctuation below the classical limit established by the Poisson photon statistics for coherent light. We will discuss the development of nonclassical light sources. Of most interest is a single-photon source achieved by having only one QD in the active medium. Also discussed is the challenge to produce single-photons at a high rate while maintaining single-photon purity. Section IV describes how CQED effects in devices may be modeled. An overview of models of diverse levels of sophistication is given. These are microscopically based fully quantized models, where both active medium and radiation field are treated quantum mechanically. Furthermore, device behavior is described in terms of electrons and holes occupying states of a nanostructured semiconductor. Finally, Sec. V summarises the review and provides an outlook.

## II. REVISITING LASER PHYSICS

### A. Towards smaller lasers

Lasing is well understood in conventional lasers. For semiconductor lasers, the most in use today and the largest in size are in-plane lasers. They typically measure  $1\ \text{mm} \times 10\ \mu\text{m} \times 0.1\ \mu\text{m}$ . The longest dimension is the resonator axis, which lies in the plane of the semiconductor substrate. Also called edge-emitting lasers, they are commercially

available and can deliver constant wave (cw) power up to tens of watts per laser.

There are many applications requiring much less power, and therefore, much smaller lasers. Also regard as conventional are microlasers, such as vertical-cavity surface-emitting lasers (VCSELs), where size is drastically reduced by rotating the resonator axis perpendicular to the substrate. The result is cavity dimensions decreasing to  $\sim 1\ \mu\text{m} \times 10\ \mu\text{m} \times 10\ \mu\text{m}$ . VCSELs are the second most used semiconductor lasers today. Even in second place, there are over  $2 \times 10^9$  VCSELs in use and roughly  $100 \times 10^6$  VCSELs are produced each year to keep up with ever increasing demand.

A goal in semiconductor laser development is to continue reducing laser size. A major motivation is to integrate more lasers onto a chip, with each laser using less energy. There is a never satisfied desire for less energy consumption. For example, optical interconnects connecting computers to make the internet and search engines function run at about picojoules per bit. The goal now is to reduce to attojoules per bit to keep up with future user demands.<sup>4</sup>

To meet that goal, advances in semiconductor nanofabrication have ushered in a new class of smaller light sources. These devices operate with nanocavities with optical mode volumes  $\approx (\lambda/2\pi n_b)^3$ , where  $\lambda$  is the lasing wavelength and  $n_b$  is the cavity background refractive index.<sup>5</sup> Reducing volume decreases the number of optical modes within a wavelength range. The challenge to size reduction is tighter optical mode control. Most approaches are based on having higher refractive index contrast between intracavity and surrounding regions. This is achieved using semiconductor/air or semiconductor/metal interfaces to form micropillars, photonic-crystal cavities, nanobeam cavities, microdisks, and coaxial cavities.<sup>6,7</sup> Lasers operating with these different cavity configurations have been demonstrated. Emission is normal to the substrate (surface emission) for some of the configurations and in-plane with the substrate for others, thus providing flexibility to serve a broad range of applications. When researching the literature, it is useful to note that some nanocavities are still referred to as “micro,” especially when the approaches originated with fabrication of microcavities.

## B. Channeling spontaneous emission

Sub-wavelength cavities exhibit unique and useful properties that are not present in larger ones. Most notable is the greater control of spontaneous emission prior to lasing because of larger frequency separation between adjacent cavity modes. The efficiency in channeling of spontaneous emission into desired modes may be quantified by the spontaneous emission factor<sup>8</sup>

$$\beta \equiv \frac{\text{Spontaneous emission rate into lasing mode}}{\text{Total spontaneous emission rate}}, \quad (1)$$

where the typical value for semiconductor lasers is  $\beta \approx 10^{-4}$ . Having significantly fewer cavity modes within the spontaneous emission spectrum means larger spontaneous emission factor. Presently, the capability exists to approach the ultimate limit, where all spontaneous emission is channeled into a single mode ( $\beta = 1$ ). One then has the potential to achieve the lowest lasing threshold and highest efficiency for a given active medium. This makes high- $\beta$  lasers attractive for many applications. The possibility for low threshold and high efficiency make it a strong candidate for optical interconnects in energy demanding applications such as the internet and search engines. With single-photon generation (which will be discussed in more detail later), QD high- $\beta$  light sources can help maximize the photon-generation rate while maintaining the quantum nature of emission purity. There is even an idea for versatile and efficient lighting based on combining the high- $\beta$  cavity's efficient channeling of radiation prior to lasing with the clamping of nonradiative losses during lasing.<sup>9,10</sup>

We emphasize the difference between single-mode lasing and  $\beta \approx 1$  operation. With large mode volume and resulting small  $\beta$ , single-mode operation arises from mode competition after lasing threshold is reached. Prior to lasing, spontaneous emission is distributed, and therefore lost, among many cavity and free-space modes. With nanocavities possessing  $\beta \approx 1$ , almost all emission (spontaneous and stimulated) is channeled into the lasing mode, both prior to and after the onset of lasing.

This recently realized ability to control spontaneous emission via  $\beta$  gives new directions to laser research and engineering.<sup>11</sup> There is the excitement of significantly reduced power consumption. Having  $\beta \approx 1$  also gives rise to several much-discussed laser physics questions, motivated by experiments indicating changes in the transition from spontaneous emission to lasing. For example, the lasing threshold becomes ambiguous, when one uses the typical criteria of input-output characteristics and linewidth narrowing. There is also a much-debated claim of thresholdless lasing.<sup>12</sup> Subsection IIC considers how these issues may be resolved with the help of quantum optics.

## C. High- $\beta$ lasing

We start with a conventional laser cavity, which has many cavity modes besides the lasing mode within the spontaneous emission spectrum. With the resulting small  $\beta$ , the transition from spontaneous emission to lasing appears as a distinct jump in the output versus input power curve [see

solid black curve in Fig. 2(a)]. This jump indicates the transition of emission from predominantly spontaneous emission to predominantly stimulated emission. When sufficiently abrupt, it precisely locates the lasing threshold, i.e., the pump power at the onset of lasing.

When  $\beta$  is increased, e.g., by operating with micro- or nanocavities, the mode spacing increases, resulting in fewer cavity modes within the spontaneous emission spectrum. With less spontaneous emission lost to nonlasing modes, the lasing threshold is lower as depicted by the other curves in Fig. 2(a). In the limit of only one mode inside the spontaneous emission spectrum, all emission (spontaneous and stimulated) is channeled into that mode and  $\beta$  becomes unity. A result is that the intensity jump marking the lasing threshold disappears completely (dotted-dashed curve).

To isolate the effects of  $\beta$ , the calculations are performed assuming perfect carrier injection  $\eta = 1$  and absence of non-radiative carrier losses  $\gamma_{nr} = 0$ . Carrier injection losses ( $\eta < 1$ ) leads to a rescaling of the pump power. With non-radiative losses, a change in slope appears at the lasing threshold for the  $\beta = 1$  curve.<sup>13</sup>

Further confirmation of lasing usually comes from narrowing of the emission linewidth with the increase in the excitation. Figure 2(b) shows that the linewidth starts at the passive cavity width (flat portion). After reaching lasing

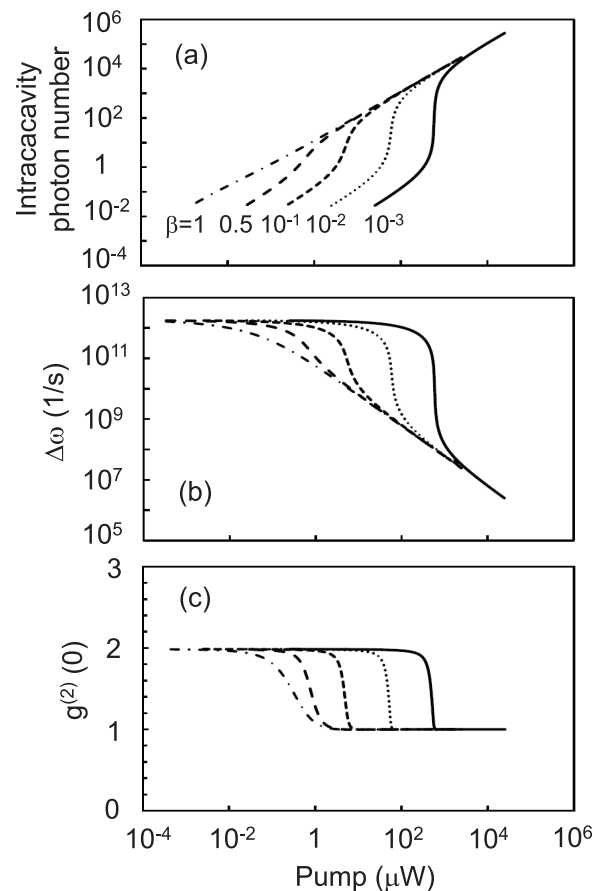


FIG. 2. Excitation dependences of (a) photon number, (b) emission linewidth, and (c) equal-time photon correlation for different values of spontaneous-emission factor  $\beta$ . The curves are obtained by numerical simulations using a cavity quantum electrodynamics (CQED) laser model described in Sec. IV and device parameters listed in the first row of Table I.



threshold, it settles (gradually or abruptly, depending on  $\beta$ ) to an excitation dependence described by the Schawlow-Townes formula.<sup>14</sup> Similar to Fig. 2(a), the drop in linewidth, and consequently, the precision in locating the lasing threshold degrades with increasing  $\beta$ . With  $\beta = 1$ , the drop vanishes all together, making the locating of lasing threshold impossible without knowing how much narrowing is sufficient to claim lasing.

An answer may come from photon statistics.<sup>15</sup> It is well known to the quantum optics community that a fundamental difference between radiation from lasing and nonlasing sources is in the nature of photon number fluctuations.<sup>16,17</sup> Laser or coherent radiation is described by Poisson statistics, while a non-lasing source emits radiation described by a thermal or Planck's statistics. With the measurement or calculation of the full photon statistics being non-trivial, the equal-time second-order photon auto-correlation function

$$g^{(2)}(0) = \frac{\langle n^2 \rangle - \langle n \rangle^2}{\langle n \rangle^2} \quad (2)$$

is often used as an alternative. In Eq. (2), the numerator is the variance in photon number and  $\langle n \rangle$  is the average photon number. For a Poisson distribution,  $g^{(2)}(0) = 1$ , while Planck's distribution has  $g^{(2)}(0) = 2$ . Nonclassical light, which will be discussed in Sec. III, is characterized by  $g^{(2)}(0) < 1$ .

Figure 2(c) shows a plot of  $g^{(2)}(0)$  versus pump. For every  $\beta$ , the transition from thermal to coherent emission with increasing excitation is clearly indicated by a drop in  $g^{(2)}(0)$  from 2 to 1. It is interesting to note that unlike the curves for input-output and linewidth narrowing, a transition region exists for  $\beta = 1$ , which locates a finite lasing threshold (when  $g^{(2)}(0) \approx 1$ ) and highlights the fact that a "thresholdless laser" still requires finite pump power to enter the regime of coherent emission of light. A similar result was reported quite some time ago, in an AMO study where CQED calculations were performed assuming a 2-level active medium.<sup>18</sup>

Returning to the question of the degree of linewidth narrowing resulting from lasing, we combined Figs. 2(b) and 2(c) to arrive at Fig. 3, where the abscissa is the deviation from the Poisson statistics value of  $g^{(2)}(0) = 1$ , which is approached only with infinite excitation. The curve suggests a narrowing to less than 2% of the passive cavity linewidth as a conservative indication of onset of lasing. More interesting is that the curve is independent of  $\beta$ , i.e., all the curves in Fig. 2 condense to one curve when plotted as in Fig. 3. We have also modeled sources with different device parameters, such as cavity Q and QD density, and found the results to be all describable by Fig. 3.

#### D. Lasing and the intracavity photon number

The condensation of results achieved in Fig. 3 motivated a search for a physical parameter or set of physical parameters that controls the transition from spontaneous emission to lasing. A first hint comes from combining Figs. 2(a) and 2(b) to give a plot of linewidth narrowing versus average intracavity photon number. All the curves for different  $\beta$ 's

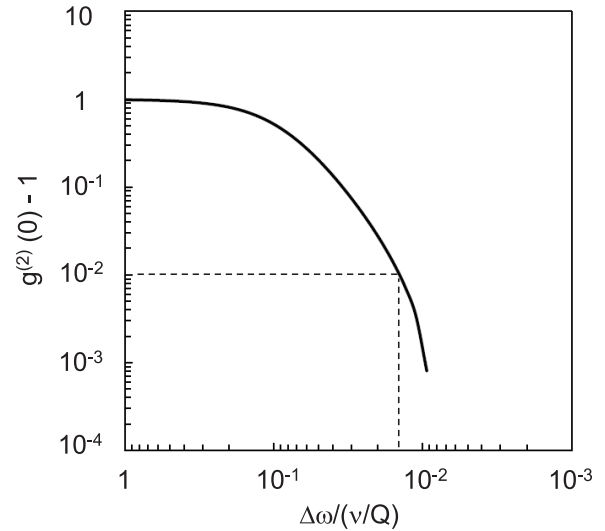


FIG. 3. Deviation from Poisson statistics versus linewidth narrowing, calculated for values of  $\beta$  in Fig. 2. Other parameters are as listed in the first row of Table I. The dashed lines indicate the linewidth narrowing necessary to be within 1% of the Poisson distribution value of  $g^{(0)}(0) = 1$ .

overlap, giving the single curve in Fig. 4(a). Figure 4(b) shows the combination of Figs. 2(a) and 2(c) to produce a plot of  $g^{(2)}(0)$  versus average intracavity photon number. Again, the curves for different  $\beta$ 's overlap one another.

To see the extent the theoretical prediction of laser behavior is supported by experiment, in Fig. 4, we plotted the measured data from five QD-based light sources, ranging from nonlasing to lasing devices. The device parameters are summarized in Table I. Each pillar consists a single InGaAs QD active layer and a high-Q microcavity with lower and upper AIAs/GaAs DBRs of 25 and 30 layered pairs, respectively (see Fig. 1). Further details on the device configuration and processing may be found in Ref. 19. The measurements were performed with the micropillars in liquid-helium flow cryostat at 10 K temperature and excited with a constant wave (cw) titanium:sapphire laser tuned to resonate with the QD wetting layer. The conversion from detector counts to intracavity photon number is made by fitting to curves such as shown in Fig. 2(a).

In Fig. 4(a), the experimental data overlap very well with the calculated curve, and hence, strongly support the claim of sole dependence of linewidth narrowing on intracavity photon number. In Fig. 4(b), the measured data are more scattered, especially at low photon number. This is caused by the conflicting demands of long collection time to compensate for the low signal and need for sufficient time resolution (or longer coherence time) to pinpoint the zero-delay value. A consequence is an underestimation of  $g^{(2)}(0)$  at thermal light conditions. Nevertheless, the measurement shows a trend that is consistent with the calculated curve.

The consolidation of results depicted by Fig. 4 indicates that laser (or non-laser) action comes solely from achieving a certain photon number inside the optical cavity. Other factors, such as cavity configuration, active medium, and carrier transport, enter only in that they affect the intracavity photon number. This is a helpful result for laser engineers because there is considerably more expertise in maximizing

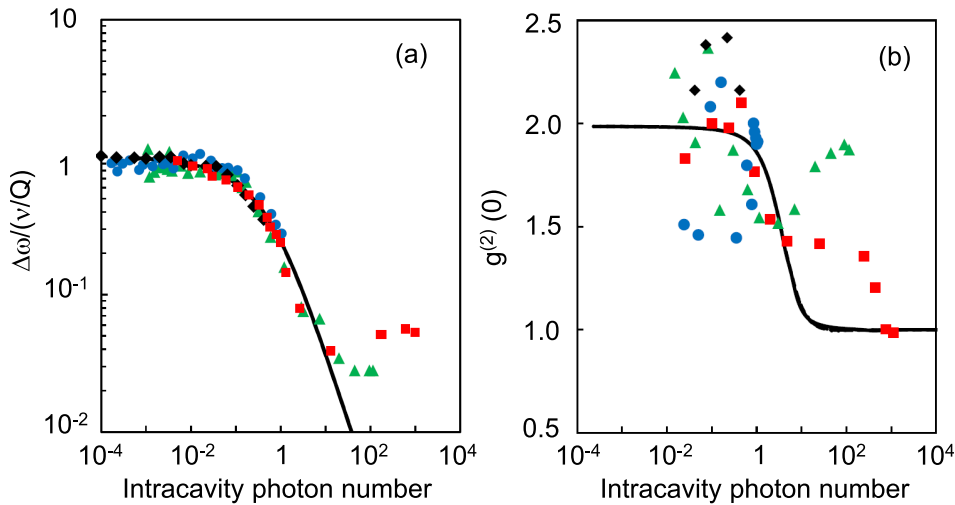


FIG. 4. (a) Linewidth narrowing and (b)  $g^{(2)}(0)$  versus intracavity photon number. The curves are calculated using the parameters in first row of Table I. All the curves for  $\beta = 10^{-3}$  to  $\beta = 1$  overlap. The experimental points are for the cavity-enhanced light sources with parameters listed in rows 2–5 of Table I. Reprinted with permission from S. Kreinberg *et al.*, *Light: Sci. Appl.* 6, e17030 (2017). Copyright 2017 Nature Publishing Group.<sup>5</sup>

intracavity intensity than in controlling abstract properties such as photon correlation.

While the plots in Fig. 4 improve our understanding of lasing, they also expose behaviors that are presently not completely understood. For example, from radiation field quantization, we understand that having more than one photon will cause the onset of stimulated emission, and hence of the start of the lasing transition. However, we have yet to have an answer for the number of photons necessary to completely convert from a thermal distribution to a coherent one, i.e., from  $g^{(2)}(0) = 2$  to  $g^{(2)}(0) \approx 1$ . There is also the question of whether Fig. 4 shows the fundamental limit. The curves are obtained assuming that inter-QD correlations are negligible, which is true for present lasers. An interesting and useful question is whether these correlations, which have been shown to give rise to interesting quantum optical phenomena, such as superradiance, can be exploited to produce a new class of ultra-low-threshold lasers. Superradiance will be discussed further in relation to inter-QD correlations in Sec. IV.

### III. QUIETING PHOTON STATISTICS

In Sec. II, we show how one started with improving laser performance and ended up having to resort to quantum optics to understand the results. In this section, we describe a

TABLE I. Parameters for nano- and micropillars used in study.<sup>a</sup>

	$\emptyset$ ( $\mu\text{m}$ )	Q	$\beta$	$N_{\text{QD}}$	$\eta$	
Calculation	0.1	10 000	$10^{-3}$ –1	10	1.0	...
A	1.7	8300	0.40	10	0.36	Black diamond
B	2.0	32 100	0.37	6	0.36	Blue circle
C	2.0	32 100	0.37	15	0.18	Green triangle
D	2.5	22 800	0.23	60	0.017	Red square

<sup>a</sup>The columns are (left to right) pillar diameter, cavity Q, spontaneous emission factor  $\beta$ , effective number of QDs interacting with the cavity field  $N_{\text{QD}}$ , and injection efficiency  $\eta$ . The first row lists input parameters for the nanolaser calculated curves in Figs. 2–4. The other rows are device parameters for the experimental QD-micropillar lasers. They are either measured directly or extracted from fitting experimental data to the CQED model.

different situation, where the use of quantum optics is intended right from the beginning to enable a new class of light sources for entirely new applications. Novel to optoelectronics is the generation of nonclassical light for applications that require regularity in spontaneous emission, rather than the naturally occurring randomness. The nonclassical-light source that is a key component in the realization of optical processing of quantum information, such as cryptography, computing, and communication, is the single-photon source. With complete photon antibunching, fluctuations in photon number (photon statistics) are reduced to the stage where only one photon is emitted at a time. This section starts with a review of the types of light (thermal, coherent, and nonclassical), and then move on to a discussion of CQED considerations involved with developing sources of high single-photon flux and purity.

#### A. Types of light

Figure 5 shows ways of thinking about the types of light.<sup>20</sup> For a large signal, the classical picture is that of intensity and its fluctuations in time (first row). When the signal is very weak, one counts photoelectrons emitted by a detector. A one-to-one correspondence between photoelectrons and photons gives the picture depicted in the second row. The actual measurement involves repeatedly counting the number of emitted photoelectrons within some set time interval (time bin). With the information, one is able to plot the probability of finding a certain number of photons versus the number of photons, i.e., the photon statistics (row 3). When a complete picture provided by the photon statistics is unnecessary, one may condense the information to a normalized photon number variance, which is  $g^{(2)}(0)$  in Eq. (2).

The first column in Fig. 5 is for thermal light. It is noisy, with intensity spikes and nulls. In quantum optics language, one sees photons arriving in groups (photon bunching), as illustrated in the second row. The photon statistics is described by an exponential function, which gives a  $g^{(2)}(0) = 2$ . Until recently, we in optoelectronics think of laser light as the highest quality of light possible and we refer to it as coherent light

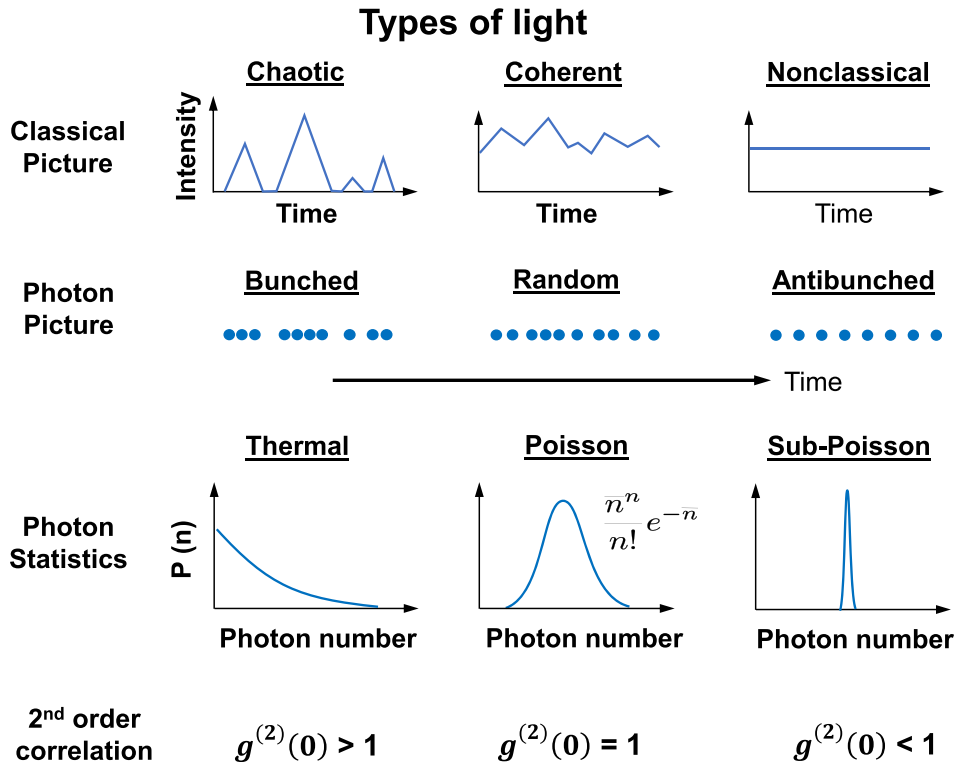


FIG. 5. The columns list the types of light and the rows show how they may be distinguished from one another.

(column 2). However, there is still noise resulting from randomly, spontaneously emitted photons especially in high- $\beta$  lasers. The resulting photon number fluctuation approaches that described by a Poisson distribution, where  $g^{(2)}(0) = 1$ . Lastly, the influence of quantum optics in optoelectronics has led to interest in another kind of light source, the nonclassical-light source. As sketched in the third column, the photons are more spread out (antibunched). In the limit of a single-photon source, photons always appear one at a time, giving  $g^{(2)}(0) = 0$ .

## B. Single-photon generation

Schemes for generating single photons range from the early experiments involving atomic and ionic beams to parametric down conversion and defect centers in crystals. Of these, using only one emitter (e.g., one InAs QD) gives perhaps conception-wise the cleanest path to a single-photon source. A single 2-level emitter can only deliver one photon at a time. However, the high single-photon purity, usually gauged in terms of a low  $g^{(2)}(0)$  value, is achieved at the cost of a low repetition rate that is determined by the free-space spontaneous emission rate. For a semiconductor QD in a heterostructure, which is a strong candidate for single-photon sources because of the advantages of electrical excitation and chip integration, this rate is at best in sub GHz range. Also serious is the lack of directionality in the spontaneous emission, which drastically reduces collection efficiency by the detector optics.

### 1. Cavity enhancement

Spontaneous emission rate and directionality have been demonstrated to improve by placing the single emitter in an optical cavity. Figure 6 depicts the cavity enhancement process. Without a cavity, the emitter radiates isotopically at a

spontaneous emission rate  $\gamma_{free}^{sp}$ , populating photon states with dispersion determined by free space [Fig 6(a)]. Under the influence of an optical cavity, the photon states are those of a combined cavity/free-space system [Fig 6(b)]. There are discrete energy states residing primarily within the cavity and states forming a continuum that reside mostly outside the cavity, i.e., in free-space. In this review, we discuss experiments with micropillars of sufficiently small cavity dimensions so that the combined cavity/free-space system has one discrete mode (the fundamental mode or FM) and a continuum of lossy modes. For these experiments, a gauge of cavity effectiveness may be obtained from a generalized version of the Purcell factor

$$F = \frac{\gamma_{mode}^{sp}}{\gamma_{free}^{sp}}, \quad (3)$$

which compares emission rate into the one discrete cavity mode to total spontaneous emission rate without a cavity. Equation (3) is a broader interpretation of the original Purcell definition (customarily denoted by  $F_p$ ) defined for an optimally matched (spectral, spatial, and polarization) emitter/cavity combination.<sup>21</sup>

### 2. Single-quantum-dot devices

The single-photon sources we studied each has an InAs QD inside a small  $3\mu\text{m}$  diameter micropillar. Each micropillar has 15 and 25.5 mirror pairs for upper and lower DBRs, which results in moderate cavity quality factors of  $2000 < Q < 3000$ . The device fabrication uses deterministic processing by means of *in-situ* optical lithography. First, one uses photoluminescence mapping to locate suitable QDs based on emission intensity, wavelength and perhaps other secondary

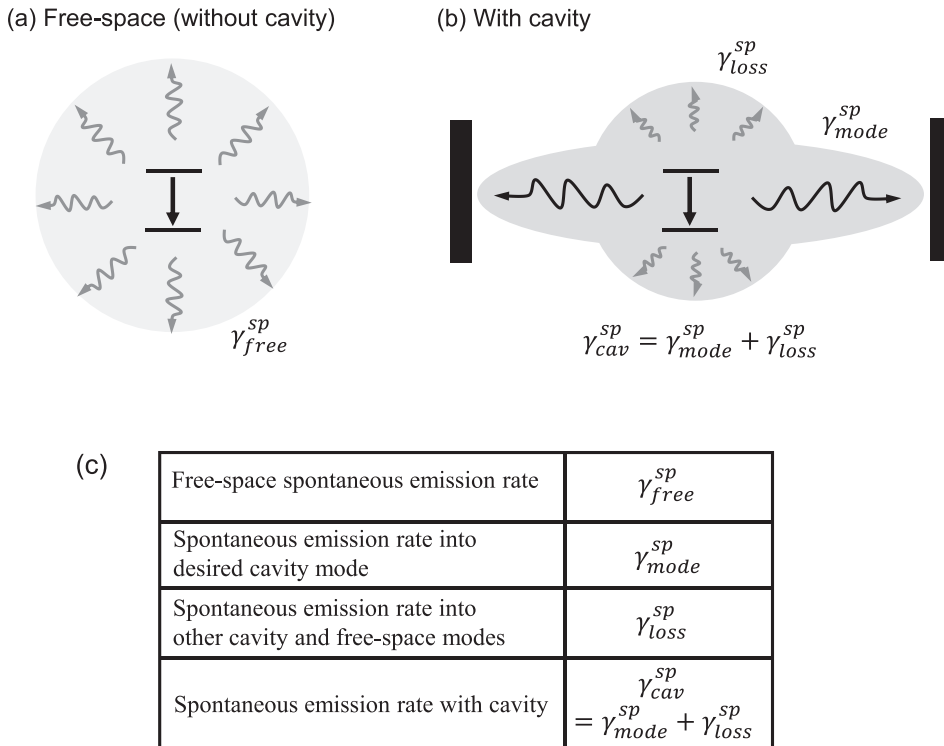


FIG. 6. Sketches showing changes in the contributions to the emission rate from (a) without to (b) with cavity. The dark wavy lines represent spontaneous emission channeled into cavity modes, while the grey ones represent spontaneous emission that rapidly leak out of the cavity into free-space. (c) Spontaneous emission rates for evaluating cavity enhancement.

details. Then optical lithography is used to pattern pillar cavities that are spatially and spectrally aligned with the selected QDs. Then, we temperature fine tune as in Fig. 7(a). Using *in-situ* optical or electron-beam lithography, single-QD devices can be processed with a yield >90%.<sup>22</sup> The standard lithographic process, which lays out the cavities using regular arrays and without as careful alignment to QD, reports yield <1%.

Figure 7 shows how the Purcell factor (henceforth, we drop “generalized”) may be determined for a device. First, the single-QD resonance is temperature tuned to match that of the micropillar fundamental mode [red trace, Fig. 7(a)]. The decay of spontaneous emission under short-pulsed excitation is recorded [red data points, Fig. 7(b)]. Then, the measurement is repeated with a large detuning between QD and micropillar resonances. The blue data points in Fig. 7(b) are

for detuning of 2.7 meV, which is sufficiently large for the spontaneous emission decay to approximate that without a cavity. When the data are fitted to exponential functions (solid curves), decay rates,  $\gamma_{mode}^{sp} = 6.0 \times 10^9 s^{-1}$  and  $\gamma_{free}^{sp} = 8.8 \times 10^8 s^{-1}$  are extracted, which gives a Purcell factor of  $F = 6.8$ , or a roughly 7-fold increase in spontaneous emission rate compared to the free-space value.

The evaluation of single-photon source performance is more complicated than that of lasers. For example, source performance is more tightly connected to the rest of the experimental setup because of weaker photon signal. Consequently, in addition to maximizing the spontaneous emission rate, it is important that the spontaneously emitted photon be directed into the cavity mode that can be efficiently collected by detector optics.<sup>24,25</sup> The extraction efficiency is introduced to quantify this requirement<sup>26</sup>

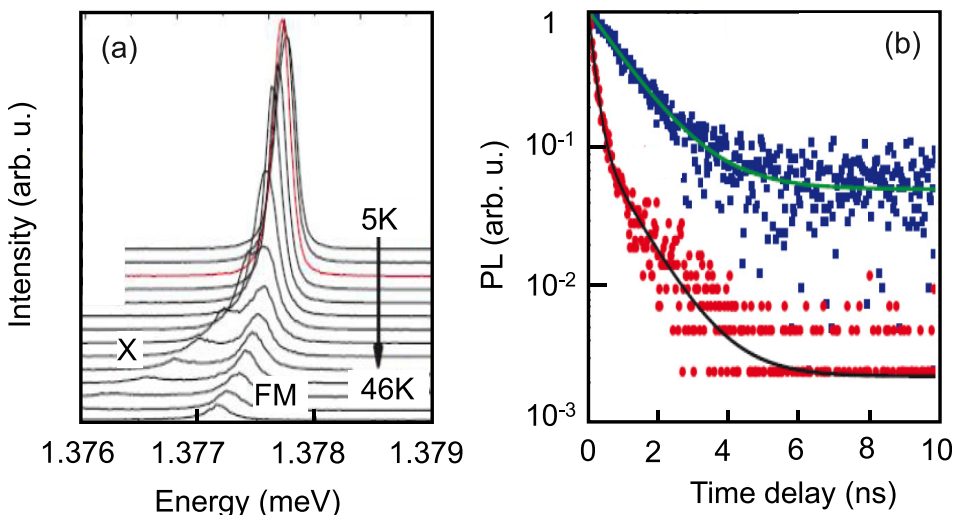


FIG. 7. (a) Spontaneous emission spectra for a single-QD-micropillar device at different temperatures. The QD resonance is denoted by X and the micropillar pillar fundamental mode is denoted by FM. The red trace is for the temperature where the QD resonance is tuned to the micropillar fundamental mode. (b) Photoluminescence signal versus time for detunings  $\Delta = 0$  and 2.7 meV (blue and red points, respectively). The points are from experiment and the curves are exponential fits. Reprinted with permission from S. Unsleber *et al.*, Opt. Express 24, 8539 (2016). Copyright 2016 OSA Publishing.<sup>23</sup>



$$\eta_{ext} = \beta\eta_t, \quad (4)$$

where  $\eta_t$ , involving photon transport between source and detector, is the fraction of photons emitted into fundamental mode that ends up collected by the first lens (with given numerical aperture, NA) in the detection path. The spontaneous emission factor

$$\beta = \frac{\gamma_{mode}^{sp}}{\gamma_{mode}^{sp} + \gamma_{loss}^{sp}} \quad (5)$$

is changed from Eq. (1) so that it applies to both lasers and nonlasers such as single-photon sources. One then defines an overall device efficiency, giving the probability of detecting a photon per excitation pulse

$$\eta_{sps} = \eta_{excitation}\eta_{ext}, \quad (6)$$

where  $\eta_{excitation}$  is the probability of emitting one photon with one excitation pulse.

Figure 8(a) plots the charged-coupled device (CCD) detector counts measured for different excitation pulse strengths. In the resonance fluorescence experiment, the excitation laser pulse is resonant to the QD transition, its strength is given in terms of the pulse area, and the counts are for photon flux into the first lens (NA = 0.42) of the collection optics. In this particular experiment, the pulse area was used to indicate how effective a laser pulse was able to invert the QD population, with  $\pi$  indicating total inversion. In the optical Bloch picture<sup>27</sup> of coherent transient in light-matter interaction, a 2-level system may be converted from entirely in the ground state to totally in the excited state by a laser pulse with area  $\pi$ . In Fig. 8(a), the experimentalist assumed that the peak of the CCD count rate is from a totally inverted system and so assigned the excitation laser pulse area of  $\pi$ . The plot shows a maximum single-photon flux of 1.3 MHz occurs with a  $\pi$  area excitation pulse. On the right y-axis is the conversion to overall device efficiency, showing that the photon flux maximum translates to an overall device efficiency of  $\eta_{sps} = 0.74 \pm 0.04$ .

There is a trade-off involving maximizing  $\beta$  and  $\eta_t$  in Eq. (4) to obtain a high the extraction efficiency  $\eta_{ext}$ . While

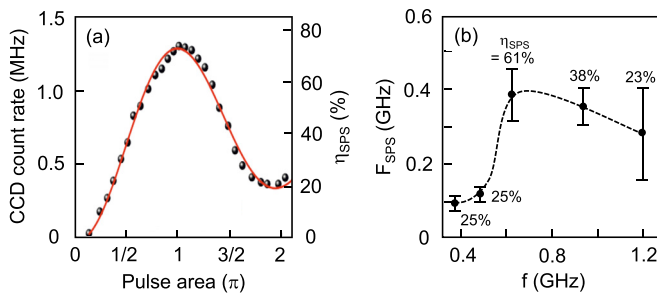


FIG. 8. (a) CCD count rate and overall device efficiency vs. pulse area for optically excited device. The red curve is drawn to connect the measured data (points). (b) Single-photon emission rate versus excitation pulse repetition rate for electrically excited device. The numbers are the overall efficiencies at various excitation rates. Reprinted with permission from S. Unsleber *et al.*, Opt. Express **24**, 8539 (2016). Copyright 2016 OSA Publishing<sup>23</sup> and from APL Photonics **1**, 011301 (2016). Copyright 2016 AIP Publishing LLC.<sup>28</sup>

$\beta$  may be made to approach unity by lowering mode volume, doing so with a smaller pillar diameter increases optical scattering at the pillar surfaces. This, in turn, degrades  $\eta_t$ , the coupling efficiency to collection optics. With careful balancing of these diametrical effects, we are about to routinely achieve  $\eta_{ext} \geq 0.7$ , with pillar diameters between  $2 \mu\text{m}$  to  $3 \mu\text{m}$  and moderate pillar Q-factors between 2000 and 3000.<sup>23</sup>

As stated earlier, compared to other candidates, a semiconductor QD has the advantage of excitation by electrical injection. This capability is very attractive if not essential for applications. There are several serious challenges, including the need for highly optimized doping schemes, mitigation of optical losses due to free carrier absorption from doping, and precise deposition of electrical contacts because of the small scale of nanophotonics elements. Figure 8(b) shows progress towards mastering these challenges. The plot is for electrically driven single-QD micropillars achieving to date some of the highest single-photon flux. Each device has an InAs QD embedded in an electrically contacted  $2 \mu\text{m}$  diameter pillar cavity with  $Q = 2100$ . From device characterization measurements, we extracted Purcell-factor  $F = 3.2$ , spontaneous-emission factor  $\beta = 0.76$ , and coupling efficiency  $\eta_t = 0.70$ . These give a photon extraction efficiency of  $\eta_{ext} = 0.53$ , which is close to the maximum overall device efficiency of  $0.61 \pm 0.10$  at 625 MHz pump repetition rate, obtained more directly from the plot in Fig. 8(b). The closeness of extraction and overall efficiencies indicates relatively efficient current injection and conversion of injected carrier to QD population,  $\eta_{excitation}$ . With our present devices, parasitic electrical effects related to a non-ideal impedance matching are responsible for the limits on  $F_{Sps}$  and  $\eta_{Sps}$  at excitation rates exceeding 625 MHz.

So far, the presented results do not confirm the generation of single-photon statistics. That was accomplished with the measurement of the second-order photon auto-correlation function,  $g^{(2)}(\tau)$ . Figure 9(a) is  $g^{(2)}(\tau)$  for the optically pumped device. At zero-time delay,  $g^{(2)}(0) = 0.0092 \pm 0.0004$ , which confirms that we have a source of very high single-photon purity at the maximum of single-photon flux. Figure 9(b) show the plots of  $g^{(2)}(\tau)$  for electrical pulse repetition rates of 373, 625, and 939 MHz. The corresponding values for  $g^{(2)}(0)$  are  $0.076 \pm 0.014$ ,  $0.149 \pm 0.021$ , and  $0.227 \pm 0.021$ , respectively. There is some degradation of single-photon purity with increase pump repetition rate. However, even at close to 1 GHz repetition rate,  $g^{(2)}(0)$  remains well below the single-photon criterium of  $g^{(2)}(0) < 0.5$ .

### 3. Emission rate versus purity

The plots in Fig. 9(b) suggest a delicate balance between photon production rate and  $g^{(2)}(0)$ . To help understand that balance, one may think of three operational cases for a single-photon source, as sketched in Fig. 10(a). In the absence of a cavity,  $g^{(2)}(0) = 0$  for all excitation, but the single-photon flux is low [case (i)]. On the other hand, a high-Q cavity may increase photon flux, but  $g^{(2)}(0)$  may suffer from the likelihood of multiple ( $>1$ ) intracavity photons

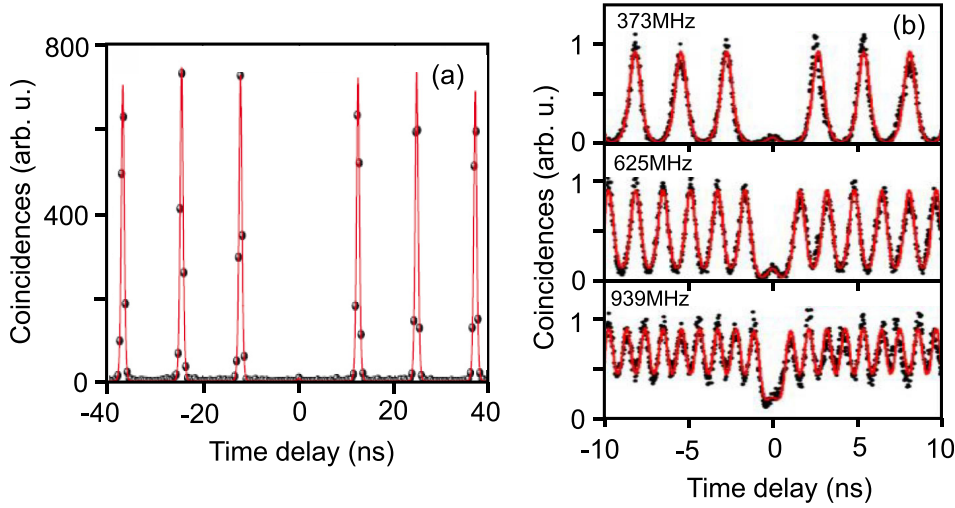


FIG. 9. (a) Counts of simultaneous detection of photons in the 2 detectors in a second-order photon auto-correlation measurement versus time delay for optical pumped single-photon source in Fig. 8(a). The excitation is with a  $\pi$  pulse area. (b) Second-order photon auto-correlation function versus time delay for electrically pumped single-photon source in Fig. 8(b). The different plots are for the excitation pulse repetition rates as labeled. Reprinted with permission from S. Unsleber *et al.*, Opt. Express **24**, 8539 (2016), Copyright 2016 OSA Publishing and from APL Photonics **1**, 011301 (2016). Copyright 2016 AIP Publishing LLC.

[case (iii)]. The challenge is to have just the right amount of cavity enhancement, so that there is no chance of having a residual photon in the cavity with an excited QD [case (ii)].

To explore how that may be accomplished, CQED calculations were performed, resulting in Figs. 10(b) and 10(c). They show the pump rate dependences of the average intracavity photon number and  $g^{(2)}(0)$  for the three cases. The curves are obtained by applying the basic model described in Sec. IV B 2 to an InAs QD in a nanocavity with light-matter coupling constant and carrier relaxation rate  $g = \gamma_r = 10^{11} s^{-1}$ , and three cavity loss rates. In curves labeled (i), a large cavity loss  $\gamma_c = 5 \times 10^{15} s^{-1}$  is used to approximate the absence of a cavity. The results show near-perfect single-photon generation,

with  $g^{(2)}(0) \approx 0$  for the entire excitation range. However, the average photon number saturates at a value much less than unity. The curves for case (ii) are computed using  $\gamma_c = 10^{12} s^{-1}$ . They indicate increases in photon number (which is good) and  $g^{(2)}(0)$  (which is bad). However, one still has a useable single-photon source because  $g^{(2)}(0) < 0.5$  all the way to saturation. (As an aside, an agreed upon single-photon criterion of  $g^{(2)}(0) < 0.5$  is motivated by

$$g^{(2)}(0) = \frac{\langle n^2 \rangle - \langle n \rangle^2}{\langle n \rangle^2} = \frac{\langle n | a^\dagger a^\dagger a a | n \rangle}{\langle n | a^\dagger a | n \rangle \langle n | a^\dagger a | n \rangle} = \frac{2}{4} \quad (7)$$

for  $n = 2$ .) To illustrate case (iii), we use  $\gamma_c = 5 \times 10^{10} s^{-1}$ . The curves show a device that is totally unusable as a single-

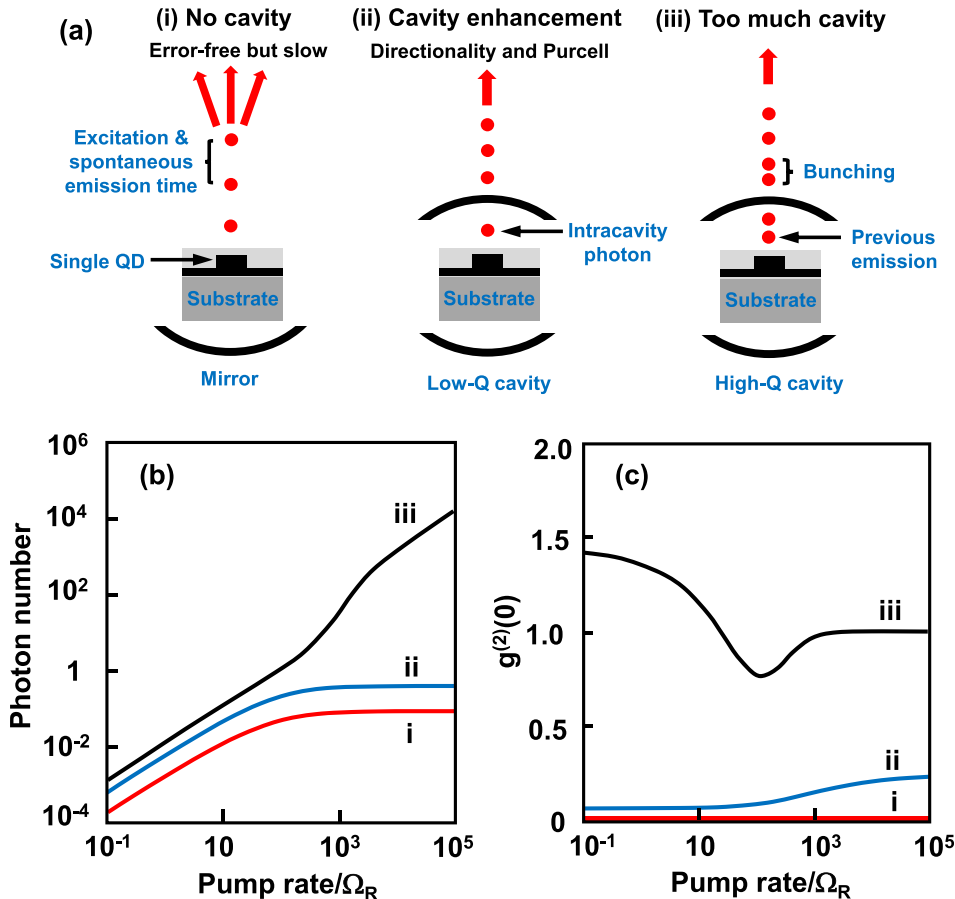


FIG. 10. (a) Progression from no cavity to too much cavity in single-photon generation: (i) single QD with back mirror to collect more emitted photons, (ii) optimum balance of cavity enhancement and  $g^{(2)}(0)$ , (iii) too much cavity when previously emitted photon remains in cavity with a re-excited QD. (b) Mean photon number and (c)  $g^{(2)}(0)$  versus pump rate for the three operational regimes in (a). The pump rate is relative to the light-matter coupling coefficient in Eq. (10). Adapted from Ref. 29

photon source regardless of pump rate. Curve (iii) in Fig. 10(c) indicates photon bunching with  $g^{(2)}(0) \sim 1.5$  at low excitation, followed by an interesting dip to  $g^{(2)}(0) < 1.0$ , indicating nonclassical photon statistics. Then, the curves predict lasing with single emitter, a much researched quantum optical phenomenon within the AMO and semiconductor communities.<sup>30,31</sup> Curve (iii) in Fig. 10(b) clearly has the ‘‘S’’ shape signature for lasing, which is confirmed in Fig. 10(c) by  $g^{(2)}(0)$  reaching unity before saturation sets in.

Figure 11 shows information that may be used to optimize a cavity for a single-photon source. To obtain such a curve, we repeated the calculations resulting in Figs. 10(b) and 10(c), for a range of cavity losses to continuously trace the progression from operation without cavity to too much cavity. Then, using the values of photon emission rate and  $g^{(2)}(0)$  at saturation, we arrived at Fig. 11(a), which indicates the attainable degree of antibunching as a function of the attainable emission rate. For example, it predicts the possibility of single-photon ( $g^{(2)}(0) < 0.5$ ) generation rates up to 30 GHz with  $\gamma_c = 10^{11} \text{ s}^{-1}$  and a pump rate of 50 GHz.

In terms of applications, one may need a more direct evaluation than indicated by  $g^{(2)}(0)$ . The process of coming up with a better gauge can be involved, because of considerations involving measurement setup or application.<sup>32,33</sup> For the present discussion, we settle on a single-photon purity, which one can calculate knowing the full photon statistics from, e.g., a density-matrix calculation<sup>34</sup>

$$\eta = \frac{p_1}{\sum_{i>1} p_i}, \quad (8)$$

where  $p_n$  is the probability of finding  $n$  photons and  $\eta^{-1}$  is the error arising from multiple photon emission. The curves in Fig. 11(b) show informative and interesting features. First, the blue curve indicates that for purity  $\eta > 10^3$ , it is necessary to ascertain that there is only one QD present, which in turn limits the emission rate to at best 30 GHz. Interesting are the red and green curves, which apply to devices where fabrication imperfections led to more than one QD within the cavity. They show that if the purity requirement is reduced to  $\eta < 10^3$ , the two or three QD devices may be

serviceable. Moreover, they produce higher emission rates than the single-QD device.

#### IV. MODELING QUANTUM OPTICAL EFFECTS

This section describes the incorporation of quantum optical physics into models for semiconductor light-sources. Using a Hamiltonian where semiconductor medium and radiation field are treated quantum mechanically, equations of motion are derived for carrier and photon populations, as well as for correlations arising from light-matter interaction. Solving these equations gives the intracavity photon number, emission linewidth and 2nd order intensity correlation. The approach improves on the earlier 2-level system treatment used in AMO studies on the effects of CQED on laser behavior. It gives a more detailed description of the semiconductor aspect, such as the presence of QD inhomogeneous broadening and the effects of the embedding quantum well (QW). More importantly, it accounts for the quantum statistics of the charge carriers. Additionally, the approach gives the emission coherence and photon correlation properties to arbitrary order via a systematic extension of the derivation to higher orders in light-matter correlations.

##### A. Hamiltonian and cluster expansion

The starting point for describing the interaction of electrons and holes in QD states with photons is the Jaynes-Cummings Hamiltonian,<sup>35</sup> modified for a semiconductor

$$H = \hbar\nu \left( a^\dagger a + \frac{1}{2} \right) + \sum_i \left( \varepsilon_i^e c_i^\dagger c_i + \varepsilon_i^h b_i^\dagger b_i \right) - i\hbar g \sum_i \left( b_i^\dagger c_i^\dagger a - a^\dagger c_i b_i \right). \quad (9)$$

In the Hamiltonian,  $\hbar\nu$  is the photon energy,  $a^\dagger$  and  $a$  are the photon creation and annihilation operators, the subscript  $i$  labels the QD,  $\varepsilon_i^e$  and  $\varepsilon_i^h$  are the single-particle QD electron and hole energies,  $c_i^\dagger$  and  $c_i$  are creation and annihilation operators for electrons, and  $b_i^\dagger$  and  $b_i$  are the corresponding operators for holes. Also in Eq. (9), the light-matter coupling coefficient is

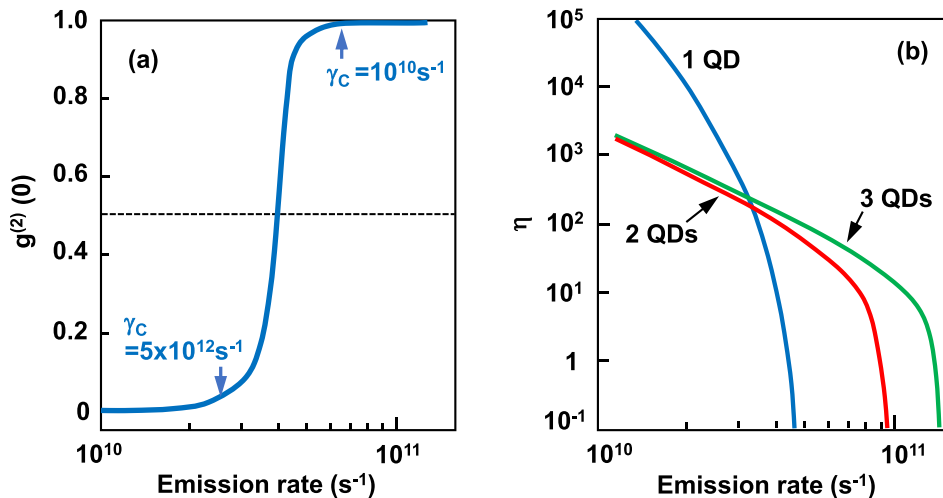


FIG. 11. (a)  $g^{(2)}(0)$  versus photon emission rate obtained from combining the results such as in Fig. 10. The curve is obtained from a series of calculations where cavity loss rate  $\gamma_c$  is varied and high excitation is used to drive the device to saturation. The emission rate is  $\gamma_c n_p$ . (b) Single-photon purity versus emission rate computed as in (a) with a model giving the exact photon statistics. Reprinted Figs. 1 and 3 with permission from C. Gies *et al.*, Phys. Rev. A **91**, 061804(R) (2015). Copyright 2015 American Physical Society.<sup>29</sup>

$$g = \wp \sqrt{\frac{\nu}{\hbar \epsilon_b V}}, \quad (10)$$

where  $\wp$  is the bulk material dipole matrix element,  $V$  is the optical mode volume, and  $\epsilon_b$  is the background permittivity. Most models assume location of the QDs at the laser mode antinode and ignore electronic structure details such as overlap of electron and hole envelope functions. We follow these assumptions in the calculations performed for this paper.

The Hamiltonian is written in a second quantized (Fock) representation for two reasons. First is that the carriers and photons are among themselves indistinguishable. Therefore, properly symmetrized (for photons) and antisymmetrized (for electrons and holes) wavefunctions are necessary. The second quantized representation conveniently takes care of the book keeping via the use of commutation relations for the photon operators and anti-commutation relations for the carrier operators, e.g.,

$$[a, a^\dagger] = aa^\dagger - a^\dagger a = 1, \quad (11)$$

$$\{c_i, c_j^\dagger\} = c_i c_j^\dagger + c_j^\dagger c_i = \delta_{ij}, \quad (12)$$

$$\{b_i, b_j^\dagger\} = b_i b_j^\dagger + b_j^\dagger b_i = \delta_{ij}. \quad (13)$$

The second reason is that absorption and emission create or annihilate photons and electron-hole pairs. This can be readily handled with second quantization by particle creation and annihilation operators.

There are many directions for proceeding. Some approaches are based closer to first-principles<sup>36</sup> and they lay the foundation for the more phenomenological ones, which are more suitable for device modeling. Figure 12 is a schematic outline of the derivation procedure that is particularly suited for incorporating details useful for device engineering. At the first (singlet) level, are the equations of motion for the

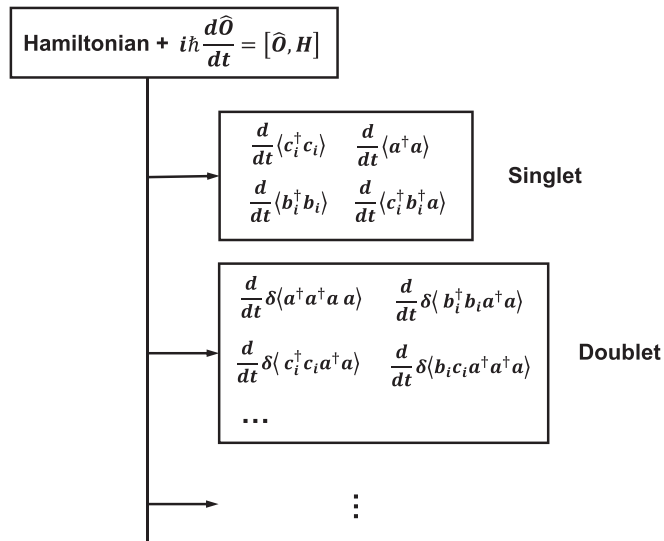


FIG. 12. A schematic outline of the approach used in deriving the equations of motion for the CQED model. The equations of motion may be derived using the Schrodinger or Heisenberg picture. The Heisenberg operator equation of motion is showed in the figure.

populations,  $n_p = \langle a^\dagger a \rangle$ ,  $n_i^e = \langle c_i^\dagger c_i \rangle$  and  $n_i^h = \langle b_i^\dagger b_i \rangle$ , and the polarization  $p_i = \langle b_i^\dagger c_i^\dagger a \rangle$ . The light-matter interaction couples these equations to expectation values of products of two single-particle operators. For example, in the case of the polarization equation of motion

$$\begin{aligned} \frac{db_i^\dagger c_i^\dagger a}{dt} &= \frac{i}{\hbar} [H, b_i^\dagger c_i^\dagger a] = i(\omega_i - \nu) b_i^\dagger c_i^\dagger a \\ &+ g \sum_j b_i^\dagger c_i^\dagger c_j b_j + g (c_i^\dagger c_i + b_i^\dagger b_i - 1) a^\dagger a, \end{aligned} \quad (14)$$

where  $\hbar\omega_i = \epsilon_i^e + \epsilon_i^h$  is the QD transition energy. Equation (14) shows that  $\langle b_i^\dagger c_i^\dagger a \rangle$  dynamics depends on the “2-particle” expectation values (doublets),  $\langle c_i^\dagger c_i a^\dagger a \rangle$ ,  $\langle b_i^\dagger b_i a^\dagger a \rangle$  and  $\langle b_i^\dagger c_i^\dagger c_j b_j \rangle$ . In turn, the equations of motion for the doublets contain “3-particle” expectation values (triplets) and so on. Consequently, the problem is described by an infinite hierarchy of coupled differential equations.

The highly nonlinear coupled differential equations can only be solved numerically, using some truncation procedure to approximately deal with the infinite hierarchy. One approach is to first normal order (creation operators to left of annihilation ones), then factorize higher-order expectation values into products of single-particle quantities,  $n_p$ ,  $n_i^e$ ,  $n_i^h$ , and  $p_i$ . For example,

$$\langle c_i^\dagger c_i a^\dagger a \rangle = n_i^e n_p + \delta \langle c_i^\dagger c_i a^\dagger a \rangle. \quad (15)$$

Keeping only correlations necessary for the determination of emission linewidth and second order intensity correlation, this Cluster expansion method provides a flexible analytical tool for modeling QD lasers. Properties of the experimental structure, such as details of carrier transport and QD homogeneity, may be included at various levels of details.

## B. Levels of detail and comparison

This subsection gives an overview of how one continues with the Cluster expansion approach to arrive at CQED models of diverse levels of sophistication. These models have in common that both active medium and radiation field are treated quantum mechanically. They differ in the microscopic details, i.e., in how the electrons and holes occupying states of a nanostructured semiconductor are treated. In the remainder of this subsection, we will show how these differences are clearly illustrated by the equations of motion for the carrier and photon populations. Other differences, regarding the treatment of the electron-hole polarization and the higher-order correlations contributing to  $g^{(2)}(0)$  will be presented in the Appendix.

### 1. Basic model

Under certain experimental conditions, such as at sufficiently low temperature, one may decouple the QW from the QDs, and only tracks the QDs interacting with the radiation



field. All carrier transport effects are approximated by an injection efficiency  $\eta$ . A further simplification comes from accounting for QD inhomogeneous broadening via a parameter  $N_{QD}$ , which is the effective number of QDs interacting with the laser field. This approach is closer to the earlier rate-equation treatments,<sup>5</sup> except that the derivation extends to include the linewidth and intensity correlation.

With the above simplifications, the Cluster expansion gives

$$\frac{dn_e}{dt} = -2gRe(p) + \eta P(1 - n_e) - \gamma_{nr}n_e - \gamma_{nl}n_en_h, \quad (16)$$

$$\frac{dn_h}{dt} = -2gRe(p) + \eta P(1 - n_h) - \gamma_{nr}n_h - \gamma_{nl}n_en_h, \quad (17)$$

$$\frac{dn_p}{dt} = 2N_{QD}gRe(p) - 2\gamma_c n_p, \quad (18)$$

$$\begin{aligned} \frac{dp}{dt} = & -[\gamma + \gamma_c + i(\omega - \nu)]p + gn_en_h + g(n_e + n_h - 1)n_p, \\ & +g(\delta\langle c^\dagger ca^\dagger a \rangle + \delta\langle b^\dagger ba^\dagger a \rangle), \end{aligned} \quad (19)$$

where the QD label “ $i$ ” is redundant and therefore dropped. In Eqs. (18) and (19), the cavity properties enter in terms of the lasing mode frequency  $\nu$  and the photon decay rate  $2\gamma_c = \nu/Q$ , where  $Q$  is the cavity quality factor. To model the complete emitter, contributions from the laser excitation, nonradiative loss and the presence of nonlasing modes are added phenomenologically into Eqs. (16)–(19). For these contributions,  $\gamma_{nr}$  accounts for nonradiative carrier loss,  $\gamma_{nl}$  is the spontaneous emission rate into nonlasing modes and  $\gamma$  is the dephasing rate. For the excitation,  $P$  is the rate of carrier injection at the cladding layers,  $\eta$  accounts for carrier transport from the cladding layers to the QDs, and  $(1 - n_\sigma)$  accounts for Pauli blocking.

## 2. Reduction to 2-rate equation limit

Equations (16)–(19) may be simplified in the rate-equation limit, when the polarization changes sufficiently fast to follow any time variation in the photon and carrier populations. As shown in the Appendix, the adiabatic elimination of the polarization then gives

$$\begin{aligned} \frac{dn_i^e}{dt} = & -2\frac{g^2}{\gamma + \gamma_c} [n_i^e n_i^h + (n_i^e + n_i^h - 1)n_p(t)] \\ & + P(1 - n_i^e) - \gamma_{nr}n_i^e - \gamma_{nl}n_i^e n_i^h. \end{aligned} \quad (20)$$

Furthermore, we define a total carrier number  $N = \sum_i n_i^e = \sum_i n_i^h$ , so that Eqs. (16) and (17) become

$$\frac{dN}{dt} = -\frac{c}{n_b} A_g(N - N_{tr}V)n_p + \eta P - \gamma_{nr}N - BVN^2. \quad (21)$$

In the above equation, we make a connection with two quantities traditionally used to characterize a gain medium: the gain coefficient  $A_g = 4g^2 n_b / [c(\gamma_c + \gamma)]$  (with dimension of inverse length) and the transparency carrier density  $N_{tr} = N_{QD}/(2V)$ , where  $V$  is the active region volume. For spontaneous emission, we choose the bimolecular description

$$BN^2 = \left(2\frac{g^2}{\gamma + \gamma_c} + \gamma_{nl}\right) \frac{1}{V} \sum_i n_i^e n_i^h, \quad (22)$$

where  $B$  [with dimension of  $1/(\text{volume}\cdot\text{time})$ ] is the bimolecular carrier recombination coefficient. Equally often the simple expression  $\gamma_{sp}N$  is used, where  $\gamma_{sp}$  is the spontaneous emission rate. The actual evaluation of  $\sum_i n_i^e n_i^h$  for QW or bulk active medium and fitting to  $\gamma_{sp}N^n$  produces  $n = 2$  at low carrier density and progresses to  $n < 2$  at high carrier density because of state filling in the presence of the Exclusion Principle.<sup>37</sup> In addition,  $P = JV/(ed)$ , where  $J$  is the injection current density,  $e$  is the electron charge and  $d$  is the active region thickness. Making the same substitutions in Eq. (18) gives

$$\frac{dn_p}{dt} = \frac{c}{n_b} A_g(N - N_{tr}V)n_p - \beta BVN^2 - \frac{\nu}{Q}n_p. \quad (23)$$

Equations (21) and (23) are the semiconductor equivalent of the two rate equations used in AMO CQED studies. They also represent the often used and highly simplified semiconductor laser rate equations. In the semiconductor laser case, the equations are usually expressed in terms of carrier and photon densities. We found that working with photon and carrier numbers makes more convenient the tracking of particle number conservation, especially for single and few QD sources, and when the active region and optical mode volumes are different. When working with photon and carrier densities, a mode confinement factor is typically introduced to account for the volume difference.<sup>2</sup> In the end, the choice is decided based more on familiarity.

## 3. QD-QW model

One may proceed in the opposite direction and extend the basic model to more accurately describe the semiconductor active region. Examples are a more detailed account of inhomogeneous broadening in QDs and carrier transport between QDs and embedding QW, where carrier injection typically occurs. These two improvements allow the treatment of nonequilibrium carrier distribution effects, such as spectral hole burning, plasma heating, and population bottleneck, at the level of carrier-carrier and carrier-phonon scattering.

The Cluster expansion now leads to

$$\begin{aligned} \frac{dp_i}{dt} = & -[i(\nu - \omega_i) + (\gamma + \gamma_c)]p_i \\ & + g[n_{e,i}^{OD} n_{h,i}^{OD} + (n_{e,i}^{OD} + n_{h,i}^{OD} - 1)n_p], \end{aligned} \quad (24)$$

$$\frac{dn_p}{dt} = 2 \sum_n n_{inh}(\omega_n) Re(gp_n) - 2\gamma_c n_p, \quad (25)$$

$$\begin{aligned} \frac{dn_{\sigma,i}^{OD}}{dt} = & -2Re(gp_i) - \gamma_{nl}n_{e,i}^{OD}n_{h,i}^{OD} - \gamma_{nr}n_{\sigma,i}^{OD} - \gamma_{c-\sigma} \\ & \times [n_{\sigma,i}^{OD} - f(\varepsilon_{\sigma,i}^{OD}, \mu_\sigma, T)] - \gamma_{c-p} [n_{\sigma,i}^{OD} - f(\varepsilon_{\sigma,i}^{OD}, \mu_\sigma^l, T_l)], \end{aligned} \quad (26)$$

$$\begin{aligned} \frac{dn_{\sigma,k}^{QW}}{dt} = & \frac{P}{N_{\sigma}^p} f(\varepsilon_{\sigma,k}^{QW}, \mu_{\sigma}^p, T_p) (1 - n_{\sigma,k}^{QW}) - \gamma_{nr} n_{\sigma,k}^{QW} \\ & - \gamma_{c-c} \left[ n_{\sigma,k}^{QW} - f(\varepsilon_{\sigma,k}^{QW}, \mu_{\sigma}, T) \right] \\ & - \gamma_{c-p} \left[ n_{\sigma,k}^{QW} - f(\varepsilon_{\sigma,k}^{QW}, \mu_{\sigma}^l, T_l) \right], \end{aligned} \quad (27)$$

where  $\sigma = e$  (h) indicates the electron (hole) populations,  $n_{\sigma,k}^{QW}$  is the QW carrier population, and  $k$  is the 2-D carrier momentum. Inhomogeneous broadening due to QD dimension or composition non-uniformity appears in the form of a QD population distribution

$$n_{inh}(\omega_i) = \frac{N_{QD}}{\sqrt{2\pi}\Delta_{inh}} \exp \left[ - \left( \frac{\hbar(\omega_i - \omega_0)}{\sqrt{2}\Delta_{inh}} \right)^2 \right], \quad (28)$$

where  $N_{QD}$  is now the actual number (resonant and non-resonant) of QDs in the active region,  $\omega_0$  is the central transition frequency of the inhomogeneous distribution, and  $\Delta_{inh}$  is the inhomogeneous width. In the numerical simulations, the QDs are grouped into bins, each with width  $\hbar\gamma$ , average transition frequency energy  $\omega_i$  and QD number  $n_{inh}(\omega_i)$ .

The above equations show the carrier injection occurring at the QW carrier population, where  $P$  is the injection rate and  $N_{\sigma}^p = \sum_k f(\varepsilon_{\sigma,k}^{QW}, \mu_{\sigma}^p, T_p)$  is the steady-state QW carrier population created by the optical or electrical excitation when all radiative processes are switched off. The injected carrier distribution  $f(\varepsilon_{\sigma,k}^{QW}, \mu_{\sigma}^p, T_p)$  is assumed to be a Fermi-Dirac function with chemical potential  $\mu_{\sigma}^p$  and temperature  $T_p$ .

The carrier capture and escape are described in terms of effective carrier-carrier and carrier-phonon scattering rates  $\gamma_{c-c}$  and  $\gamma_{c-p}$ , respectively. Scattering terms in the above equations approximate the situation where a carrier distribution is first driven to quasi-equilibrium at some plasma temperature by carrier-carrier scattering. Then, carrier-phonon scattering further relaxes the carriers to quasi-equilibrium distributions at the lattice temperature. The asymptotic quasi-equilibrium distributions are Fermi-Dirac functions  $f(\varepsilon, \mu_{\sigma}, T)$  and  $f(\varepsilon, \mu_{\sigma}^l, T_l)$ . For the carrier-carrier scattering, the chemical potential  $\mu_{\sigma}$  and plasma temperature  $T$  are computed by conservation of carrier population and energy. In the case of carrier-phonon scattering, the chemical potential  $\mu_{\sigma}^l$  is obtained from conservation of carrier population and the lattice temperature  $T_l$  is an input quantity.

#### 4. Comparison

All three models have been applied to a wide range of QD active media. When investigating QD laser physics, we often consider a simple shallow QD structure, such as  $\text{In}_{0.3}\text{Ga}_{0.7}\text{As}$  QDs embedded in a GaAs QW, where only the ground state transition is supported. To connect to applications, we typically use the case of InAs QDs embedded in a  $\text{In}_x\text{Ga}_{1-x}\text{As}$  QW, which emits in the  $1.3\mu\text{m}$  to  $1.5\mu\text{m}$  wavelength range of interest to telecommunication. Input into the calculations are the QD level energies and transition dipole

matrix elements. For the QD-QW model, the QW electron and hole band edge energies and their effective masses are also used.

A good comparison of the different models is the exercise for extracting the spontaneous emission factor  $\beta$  from experimental data. The points in Fig. 13 are measured for Emitter D in Table I. The curves are the calculated results from the three models. The simulation uses carrier-carrier and carrier-phonon scattering rates of  $\gamma_{c-c} = 10^{12}\text{s}^{-1}$  and  $\gamma_{c-p} = 10^{11}\text{s}^{-1}$ , respectively, estimated for  $T = 10\text{K}$ . They show that all three models are able to reproduce the shape of the experimental curve. Input parameters for the models change the predicted threshold pump power, which may be made to match the measured value by adjusting the injection efficiency parameter  $\eta$ . Another fitting parameter is the vertical axis scaling, i.e., the detector count to intracavity photon number conversion. On the other hand, the extent of the jump in output at lasing threshold is essentially insensitive to all input parameters except  $\beta$ . For this reason, the fitting of cQED models to log-log input-output plots of experimental data is widely used for determining  $\beta$ .

For the 2-rate-equation and basic models, the fit to experimental data is obtained with  $\beta = 0.014$  and  $0.0085$ , respectively. The extracted  $\beta$  values are essentially similar considering the preciseness of the shape fitting. More significant is the QD-QW model prediction of  $\beta = 0.21$  for Emitter D, which is significantly higher than those from the other two models.

### C. Caution: Underestimating $\beta$

#### 1. QD inhomogeneous broadening

When fitting with a scaled-down cQED model, e.g., the 2-rate-equation model, a cause for error is from ignoring the presence of QDs that are detuned from the cavity mode. They are present because fabrication imperfection leads to distributions in QD size or composition. The detuned QD nevertheless interact with the cavity field because of transition broadening from interactions between the QD and its environment, such as carrier-carrier and carrier-phonon

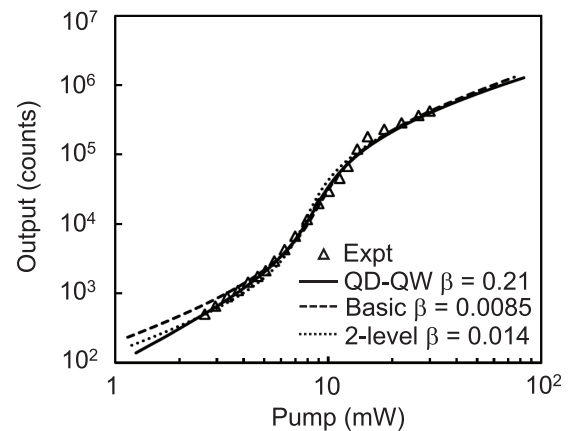


FIG. 13. Log-log plot of output versus input from experiment and from the three models described in this section. The simulations were performed with similar resonator and gain region parameters. To obtain the fit to experiment, the values of  $\beta$  were adjusted as indicated in the figure.

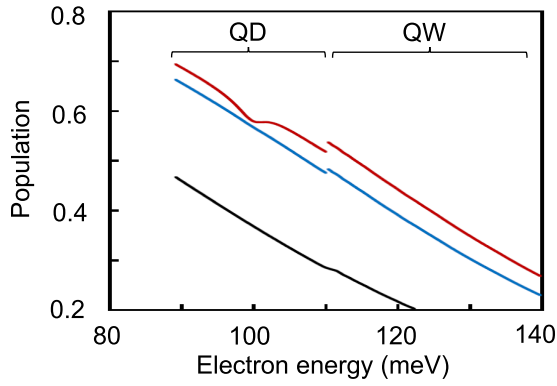


FIG. 14. Steady-state electron population per electronic state versus state energy, from the calculation giving the solid curve in Fig. 13. The pump powers are 4 mW, 7 mW, and 20 mW (black, blue, and red curves, respectively). The energy is relative to the bulk InAs conduction band edge. Note that the maximum population is unity from the Exclusion Principle.

scattering. From semiclassical laser theory, each stimulated transition is scaled by a lineshape function<sup>38</sup>

$$L(\Delta) = \frac{1}{\Delta^2 + \frac{1}{T_2^2}}, \quad (29)$$

where  $\Delta$  is the detuning frequency and  $T_2$  is the reciprocal of the polarization dephasing rate  $\gamma$  in Eq. (19). After the onset of lasing, when intracavity intensity is high, there is further broadening (power broadening) with<sup>27,38,39</sup>

$$\frac{1}{T_2} \rightarrow \frac{1}{T_2} \sqrt{1 + \frac{3T_2 I}{2T_1 I_{sat}}}, \quad (30)$$

where  $T_1$  is the population lifetime and  $I/I_{sat}$  is the laser intensity relative to its saturation intensity.

As described earlier, the QD-QW model can account for their influences. In Fig. 13, the QD-QW model fit to the experimental data was made assuming QD inhomogeneous broadening of  $\Delta_{inh} = 20$  meV [see Eq. (28)]. Figure 14 shows the steady-state electron population distribution calculated for three different excitations. The black curve at pump power far below lasing threshold may be described by a single Fermi-Dirac function, indicating equilibrium condition

within QD and QW populations, as well as between QD and QW populations. At 7 mW pump power, which is within the transition from spontaneous emission to lasing, quasi equilibrium remains within QD and QW populations. However, the discontinuity in the blue curve indicates that the QD and QW populations are not in thermal equilibrium. Here, a dynamical population bottleneck exists where carriers in the QW are not efficiently channeled to the QD states. At the even higher power of 20mW, which is after the lasing threshold, a population hole exists in the QD population (dip in red curve). Within the population hole are QDs contributing resonantly and non-resonantly to the laser field. The gain suppression with the population bottleneck prior to lasing and the enhancement of gain from the off-resonant QDs after lasing accentuates the “S” shape input-output curve. Consequently, neglecting these contributions results in underestimation of  $\beta$ .

Similar influence of off-resonant QDs is also reported in a single-photon source experiment. Figure 15 shows measured excitation dependences of intensity spectrum and  $g^{(2)}(0)$  for a device consisting one InAs QD that is resonant with a mode from a  $1.8 \mu\text{m}$  diameter pillar cavity with  $Q = 15000$ . At low excitation, the spectrum double peak with a vacuum Rabi splitting  $\approx 60 \mu\text{eV}$  occurring with  $g^{(2)}(0) \approx 0$ , indicate a single-photon source operating under strong light-matter coupling condition. This draws much attention when first observed because of the promise for higher single-photon source performance and more potential applications within quantum computing.<sup>40–42</sup> However, like the AMO counterpart, there is relatively little activity in implementing strong coupling physics in optoelectronic devices at present. Therefore, we will not dwell on it, but instead return to the  $\beta$  extraction question.

As the laser pump increases pass  $2 \mu\text{W}$ , the double peak in the  $\mu\text{PL}$  spectrum vanishes indicating a transition from strong to weak coupling. Eventually,  $g^{(2)}(0)$  reaches unity and the device lases. Judging from the pronounced “S” shape in the measured input/output curve in Fig. 16(a), one would infer a relatively low  $\beta$  for the device. On the other hand, the cavity dimensions and the presence of strong coupling point to a  $\beta$  closer to unity. The resolution comes from modeling the experiment in detail. The stimulation revealed that the

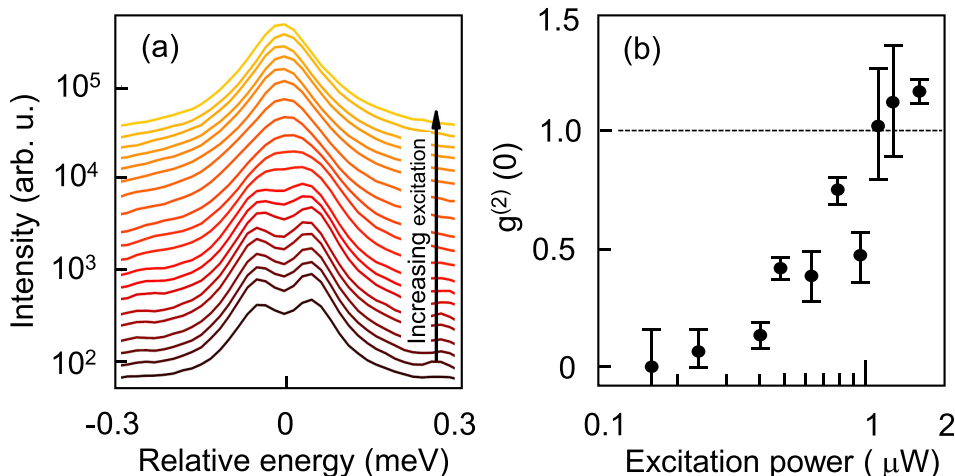


FIG. 15. (a) Measured excitation dependences of (a)  $\mu\text{PL}$  spectrum and (b)  $g^{(2)}(0)$ . Together the plots show an interesting transition from single-photon emission under strong-coupling condition to lasing in the weak coupling regime. Reprinted Fig. 3 with permission from C. Gies *et al.*, Phys. Rev. A **96**, 023806 (2017). Copyright 2017 American Physical Society.<sup>43</sup>

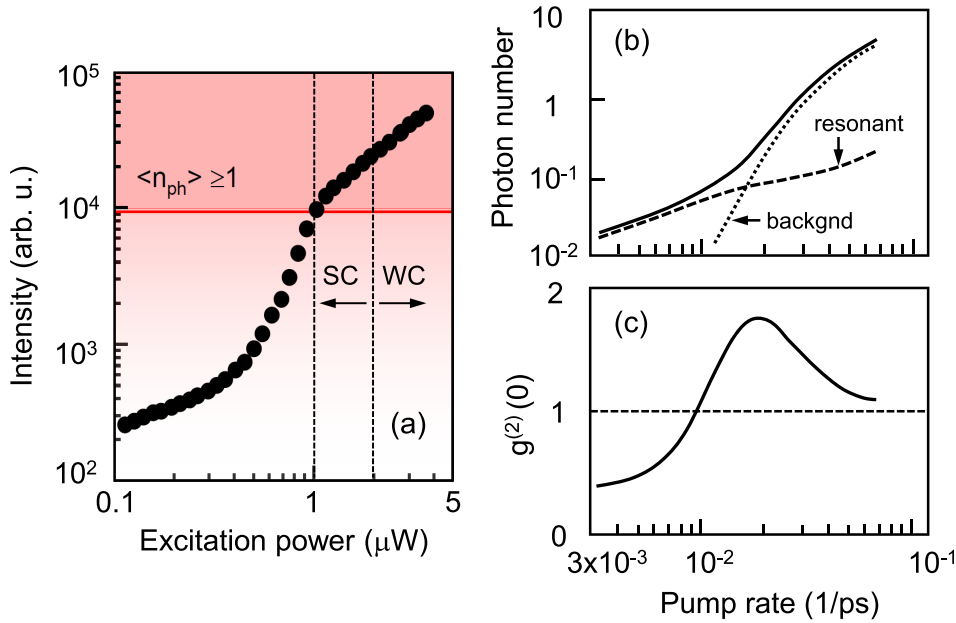


FIG. 16. (a) Measured input-output dependence. The transition from strong coupling (SC) to weak coupling (WC) is determined by the vanishing of the double peaks in the spectra in Fig. 15(a). The red horizontal line marking the onset of lasing is positioned according to when  $g^{(2)}(0) \rightarrow 1$  in Fig. 15(b). Plotted in (b) and (c) are the calculated pump rate dependences of average intracavity photon number and  $g^{(2)}(0)$ . The dashed and dotted curves in (b) are for contributions from resonant QD and from non-resonant QDs, respectively. They combine to give the “S” shape in the solid curve. The device is the same as in Fig. 15. Reprinted Fig. 3 with permission from C. Gies *et al.*, Phys. Rev. A **96**, 023806 (2017). Copyright 2017 American Physical Society.<sup>43</sup>

laser excitation at 532 nm also excited nearby, non-resonant QDs. By including the contributions from the six background QDs estimated for the sample, the fitting to experiment produces  $\beta \approx 0.22$ . As shown in Fig. 16(b), the measured “S” shape comprises two input/output curves: one from the resonant QD inside the cavity and the other from non-resonant QDs in the vicinity. Simulation shows that the resonant QD provides an average photon population of  $n_p \approx 0.2$  at saturation (dashed trace), which is insufficient to reach lasing threshold according to the discussion in Sec. IV B on laser physics. At high excitation the plot shows the onset of non-resonant QD contribution (dotted trace). The addition of resonant and non-resonant contributions then allows the device to reach lasing threshold, as in the case of the inhomogeneously broadened laser discussed in Figs. 13 and 14. There, system starts with thermal photon statistics at low excitation and with a relatively large number of QDs contributing to the emission. Here, one starts in a photon-number (Fock) state and single QD instead. However, in both cases, neglecting off-resonant QDs arising from inhomogeneous broadening results in underestimating  $\beta$ .

## 2. Inter-QD correlations

There are also cases of underestimation of  $\beta$  when inter-QD correlation is present. The correlation depends sensitively on the QD number. With a small number of QDs in the system, collisions are reduced to the extent necessary for the correlations to exist. In this situation, the electron-hole polarization receives contributions such as  $\langle b_i^\dagger c_j^\dagger c_j b_i \rangle$ , where  $i \neq j$  label the QDs. A consequence is the possibility of giant photon bunching as well as sub- and super-radiance.<sup>44</sup> We will discuss how an error can occur in the extraction of  $\beta$  from experiment.

Figure 17(a) is a plot of  $g^{(2)}(0)$  versus pump power for a device similar to Device D in Table I, except for having 40 instead of 60 QDs in the active region. The points are from experiment and the curve is calculated using the QD-QW model with inter-QD correlation taken into account. An important feature is  $g^{(2)}(0) > 2$  at low excitation, which indicates super-thermal bunching. Figure 17(b) shows the corresponding effect on the input-output curve. The solid curve labeled QD-QD is from the same calculation as in Fig. 17(a). The fit is obtained using  $\beta = 0.72$ . At first glance, the “S”

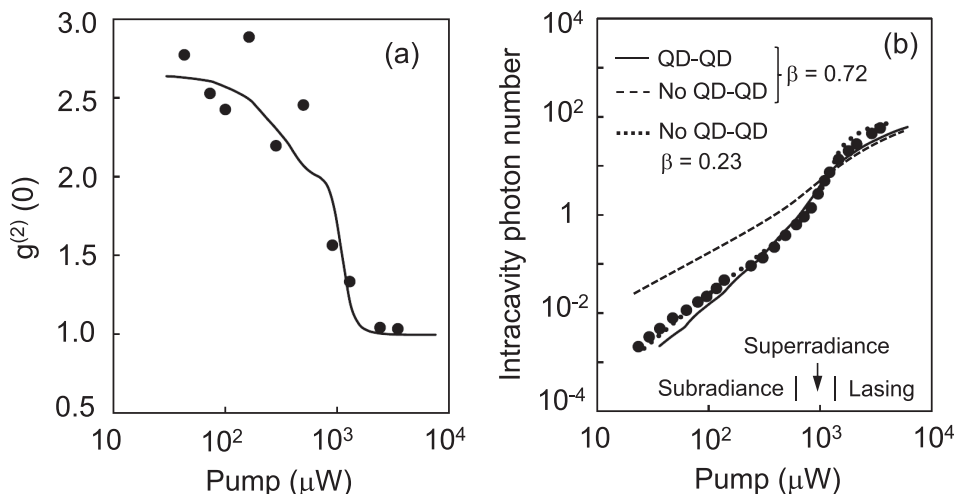


FIG. 17. (a)  $g^{(2)}(0)$  and (b) average intracavity photon number versus pump power. The points are from experiment. The curves show giant photon bunching as well as help identify sub- and super-radiance from inter-QD correlation.



looks very pronounced for a device with such a high  $\beta$ . Repeating the calculations without the inter-QD correlation gives the dashed curve, which has the flatter appearance expect with high  $\beta$ . The difference in the curves indicates the inter-QD correlation contributions. There is a region, before lasing threshold where the solid curve falls below the dashed one. Here, radiation is suppressed (subradiance). Then, at higher excitation, the inter-QD correlation switch role and enhances radiation (superradiance). With subradiance and superradiance occurring side-by-side, a pronounced “S” shape results. The dotted curve is the fit to experimental points without the inter-QD correlation. It gives  $\beta = 0.23$ , which we know is incorrect because of the unmistakable  $g^{(2)}(0) > 2$  in Fig. 17(a), indicating sub- and superradiant effects at low excitation power.

### 3. Quantum-confined Stark effect

As many of us are aware, LEDs are rapidly replacing incandescent and fluorescent lights because of advantages in durability, adaptability and environmental impact.<sup>45</sup> The LED’s efficiency in converting electricity to light allows it to be solar powered. The social impact cannot be overstated, for solar-powered LEDs enable the introduction of lighting or the replacement of health-wise dangerous kerosene lanterns in less developed and remote regions in the world.

Studies to date suggest that even higher efficiency is possible, as well as imperative for the wellbeing of the LED industry. A serious problem involves light output saturation at a very low current density of tens of A/cm<sup>2</sup>. This saturation translates to <10 mW in light output from a single LED before efficiency degrades. This concern is often referred to as the efficiency droop.<sup>46</sup>

When investigating a laser solution to the droop problem, we discovered another active medium property that may lead to an underestimation of  $\beta$ . It involves the presence of quantum-confined Stark effect (QCSE) arising from mechanical strain in certain crystal structures. For example, compared to zinc-blende crystals such as GaAs and InP, a wurtzite III-N crystal with quantum confinement along the

c-axis can have a strong strain-induced electric field.<sup>47</sup> This piezoelectric field changes the envelope functions for different QW subbands under low and high carrier densities as depicted in Fig. 18. Band structure effects in the presence of screening of QCSE is determined by solving the coupled Poisson and  $\mathbf{k} \cdot \mathbf{p}$  equations. Notice especially the change in the overlap of the ground-state electron and hole envelope functions (red curves), which significantly influences optical emission.

The appreciable change in envelope function overlap leads to significant dependence of the dipole matrix element on excitation. The dipole matrix element determining emission strength has the form<sup>13</sup>

$$\mu_{ij} = \frac{\mu_{bulk}}{2} \sum_{\sigma} \sum_n \sum_m C_{n,i} A_{m,j} \int_V d^3r u_{e,n}(r) u_{\sigma,m}(r), \quad (31)$$

where  $i$  and  $j$  are electron and hole levels involved with the optical transition,  $\mu_{bulk}$  is the bulk material dipole matrix element, the coefficients  $C_{n,i}$  and  $A_{m,j}$  account for state mixing, and the summation involving  $\sigma$  is over heavy-, light-, and crystal-split-hole states. Important to the carrier-density dependence of  $\mu_{ij}$  is the envelope function overlap, which is described by the spatial integral over electron and hole envelope functions  $u_{e,n}$  and  $u_{\sigma,m}$ , respectively, and governed by the combined effects of quantum confinement and piezoelectric field. The influence in the quantum-confined Stark effect is illustrated in Fig. 18(c), which is a plot of  $\eta = |\mu_{1,1}^{TE}/\mu_{bulk}|$  as a function of carrier density for a 3 nm In<sub>0.2</sub>Ga<sub>0.8</sub>N QW between GaN barriers.

A quick way to see the effects of Fig. 18(c) on input-output behavior is to use the 2-rate equation model. Changing  $A_g$  and  $B$  to  $\eta^2 A_g$  and  $\eta^2 B$  in Eqs. (21) and (23), we computed the curves in Fig. 19(a). For each  $\beta$ , there is a significantly larger intensity jump, and interestingly, an intensity jump remains at  $\beta = 1$ . The larger jump in photon number at threshold with QCSE comes from the suppression of intracavity photon population prior to onset of QCSE screening. This is different from the subradiance in Sec.

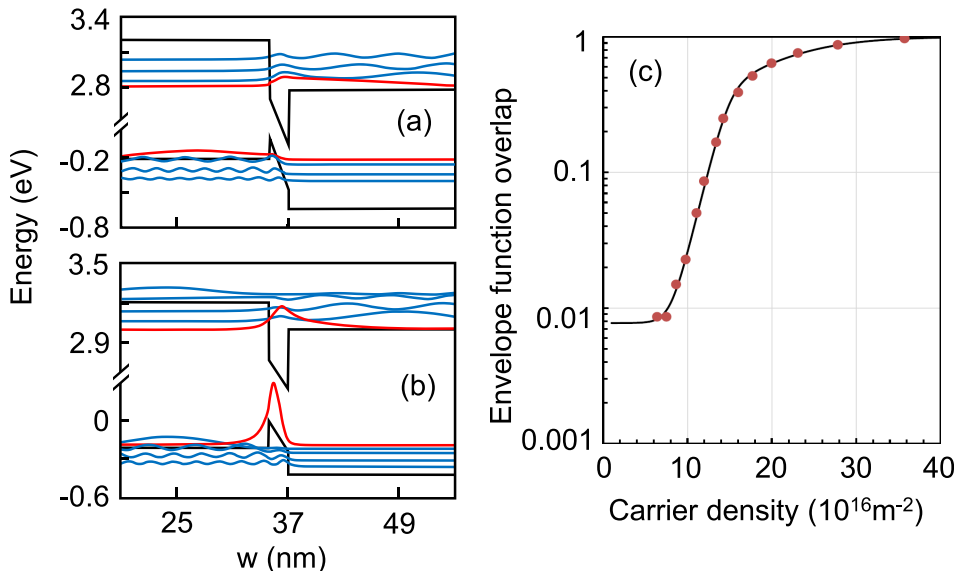


FIG. 18. Absolute square of the electron and hole envelope functions for (a) low and (b) high carrier densities. The red curves identify the envelope functions contributing to the ground state transition. The black lines plot the confinement potentials. The x-axis is along the c-axis. (c) Ground-state envelope function overlaps versus carrier density, showing importance of quantum-confined Stark effect. The curve is hand drawn to connect the points, which are computed using a Poisson and  $\mathbf{k} \cdot \mathbf{p}$  solver.

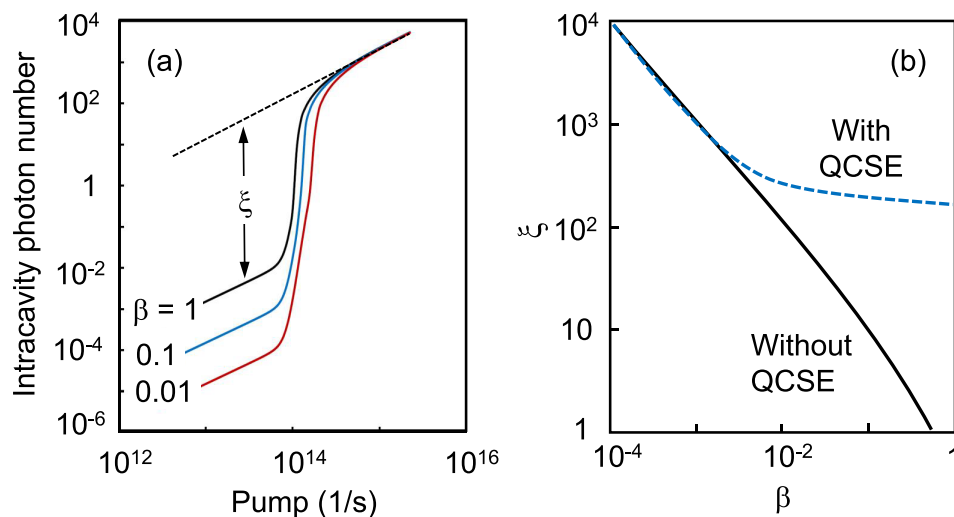


FIG. 19. (a) Input-output curves for different  $\beta$  based on Fig. 18(c) and the 2-rate-equation model. (b) A more accurate prediction of photon number jump at lasing threshold versus  $\beta$  from the QD-QW model. The solid and dashed curves are for with and without quantum-confined Stark effect, respectively.

IV C 2 in that the emission suppression is purely a single-particle effect.

In an actual device, the QCSE effect is combined with contributions from carrier capture and escape, band dispersions and nonradiative losses. We use the QD-QW model to include these contributions. Figure 19(b) summarizes the results by plotting the photon number jump at threshold  $\xi$  versus the spontaneous emission factor  $\beta$ , with and without QCSE. Comparing Figs. 19(a) and 19(b) indicates a reduction in the jump with the added contributions. The reason is the increase in lasing threshold from the added contributions, which in turn led to partial screening of QCSE prior to the onset of stimulated emission. While Fig. 19 was computed for a QD active medium, we found similar behavior, i.e., increase in photon number jump at threshold with QCSE, from calculations for InGaN QW lasers.

## V. SUMMARY AND OUTLOOK

### A. Scope

The goal we had set for ourselves was to write, as close as possible, a stand-alone introduction of quantum optics in optoelectronic engineering. Basic concepts are explained at the level of graduate level physics and electrical engineering. To accomplish that, we limited discussion to two specific examples we feel are excellent for illustrating how scientists and engineers are implementing CQED in the engineering of optoelectronic components. We complement our focused approach by citing contributions chosen from a vast literature to provide examples of the broader as well as historical perspective.

### B. Progression from physics to devices

The progression from physics idea to commercial realization involves several steps. In between, one needs to arrive at a device concept with perhaps some targeted application advantages. Then, comes the engineering development to confirm those advantages. Only afterwards will there be a possibility of sufficient interest to proceed with production engineering. In terms of the progression towards devices, the examples we used involving quantum-dot micro- and

nanocavity emitters, are passed the device conceptualization stage. While many experiments remained optically pumped, optoelectronic devices are being demonstrated.

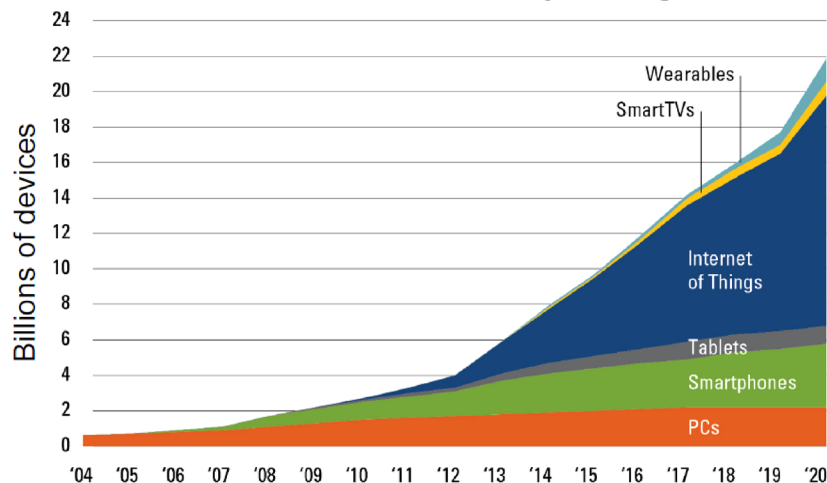
A good illustration of the progression is provided by the VCSEL. The proposal and proof of concept by Iga and his co-workers on what is today the VCSEL came in the late 1970s.<sup>48</sup> A motivation then and remains today is fully monolithic fabrication. Perhaps, one may associate the underlying physics with experiments using semiconductor etalons and superlattices to study optical nonlinearities or strong light-matter interaction.<sup>49</sup> Roughly a decade later, device research intensified, after important contributions resulting in, e.g., room-temperature cw operation, and milliampere threshold current.<sup>50,51</sup> It took until the late 1990s, after demonstration of competitiveness with in-plane lasers, e.g., in efficiency,<sup>52</sup> that engineering for production and commercialization began. Today, companies are manufacturing millions of VCSELs per year for appliances used in our daily lives.

### C. To the physicist

A physics contribution that usually comes to mind is new ideas for better devices and new applications. The single-photon source described in Sec. III is a good example. With nonclassical photon statistics, one reduces noise to the point that a semiconductor QD can be used in quantum information processing.

However, when introducing new ideas to optoelectronics, it is useful to keep in mind that there already exists a huge infrastructure. Important are compatibility with processing techniques and equipment that have been developed with considerable cost. Also important is integration into the rest of the system, including the power source and readout. Given that one has to deal with many factors beyond just coming up with a great physics idea, why would anyone be interested in device development? The answer is the lure of problems that are in urgent need for solutions. Figure 20 shows the example of expected growth in the number devices connected to the internet. Many of these devices contain optoelectronic components, which must continue to improve, e.g., in bandwidth and energy saving, to support the projected use increase.

## Forecast of the number of devices operating on the Internet



Sources: Gartner, IDC, Strategy Analytics, Machina research, company filings, BII estimates

FIG. 20. Devices (in units of  $10^9$ ) including optoelectronic ones involved with the internet versus year. The largest growth is in the “internet of things” which is a collective term for any hardware, software, data, or service that involve data transfer via the internet. (Courtesy of Jim Lott, TU-Berlin.)

### D. To the engineer

Advances in semiconductor device fabrication have enabled optoelectronic components to perform close to fundamental limitations. In some cases, understanding of the operation of these components takes the device physics into the realm of quantum optics and traditional concepts of optical gain per unit light, optical confinement, and laser operation itself are may no longer be meaningful in their design and evaluation. We hope that this review provides a timely account of the relevant quantum optics for the “traditional” device physicist and engineer who are working to adapt his or her thinking to new concepts, so as to help accelerate evolution of phenomena such as high- $\beta$  lasing and nonclassical light generation into manufacturable products.

There is another role for quantum optics besides introducing new functionalities. Not as obvious is work on device characterization and optimization. A model derived from first-principles, with a minimum of free parameters, can extract device parameters that are difficult to measure directly. Section II discusses how photon statistics in the form of intensity correlation  $g^{(2)}(0)$  can be used to distinguish between lasing and nonlasing devices in marginal cases. In Sec. IV, we describe an example where a CQED model is used to extract the spontaneous emission factor  $\beta$  from measured input-output curves.

The need for characterization also extends to the active medium. For example, with QD devices grown on silicon, threading dislocations from lattice mismatch and QD inhomogeneity from Stranski-Krastanov growth remain obstacles to be overcome.<sup>53</sup> Useful for developing growth processes is information on the inhomogeneous broadening and non-radiative carrier loss rate.<sup>54</sup> To extract these quantities from experiment requires models that treat scattering effects more rigorously than in the CQED models discussed in Sec. IV. For QWs, this means scattering contributions calculated using second-order perturbation theory, such as that resulting in the Lindblad equations. To treat QD scattering accurately, it is necessary to go beyond perturbation theory. There, quantum kinetic treatments including memory effects have been developed. For overviews on the Lindblad

and quantum kinetic approaches, see Refs. 55 and 56, respectively. The ideal device model would be one requiring only the epitaxy-growth sheet and cavity design as input.

Finally, this review is far from providing a complete picture of the impact quantum optics is or could be making in optoelectronics. Perhaps not as ready for engineering development as our chosen examples, but nevertheless intriguing for future devices are the quantum optical phenomena involving strong coupling physics, entangled-photon creation, polariton lasing, quantum coherence, and many more. Textbook discussions of these phenomena may be found in Refs. 1 and 20.

### ACKNOWLEDGMENTS

We are grateful for discussion and collaborations with C. Gies, F. Jahnke, S. Kreinberg, J. Bowers, E. Hu, T. Heindel, C. Schneider, and S. Höfling. We also thank the reviewer and M. Wanke for suggestions that make this review more readable and error free. The research was funded in part by the European Research Council under the Seventh Framework ERC Grant Agreement No. 615613 of the European Union, the German Research Foundation via the project Nos. RE2974/5-1, Ka2318 7-1, and JA 619/10-3, and the U.S. Department of Energy under Contract No. DE-AC04-94AL85000. W.W.C. acknowledges M. O. Scully and the Casper Summer Schools on quantum science and engineering for providing many ideas to connect quantum optics and optoelectronics. He also thanks the Technical University Berlin for hospitality and the German Research Foundation collaborative research center 787 for travel support.

### APPENDIX: PHOTON-CARRIER CORRELATIONS

For brevity, we left out some details involving algebra in Sec. IV B. For the interested reader, we fill in some of the gaps in this Appendix. First, the reduction to the two-rate-equation model is possible by invoking the rate-equation approximation. The assumption is basically that the polarization changes sufficiently fast to follow any time variation in the photon and carrier populations. Then, one may write Eq. (19) as

$$\begin{aligned}
p_i(t) &= g e^{-\Delta t} \int_{-\infty}^t dt_1 e^{\Delta t_1} \{n_i^e(t_1)n_i^h(t_1) + [n_i^e(t_1)+n_i^h(t_1) - 1]n_p(t_1)\} \\
&\approx \frac{g}{\gamma + \gamma_c} \{n_i^e(t)n_i^h(t) + [n_i^e(t)+n_i^h(t) - 1]n_p(t)\},
\end{aligned} \tag{A1}$$

where we reinserted the QD label “ $i$ ” in order to define the total carrier number  $N = \sum_i n_i^e = \sum_i n_i^h$ . Substituting Eq. (A1) into Eq. (16) gives Eq. (20) in Sec. IV B

Next, for the second order intensity correlation

$$g^{(2)}(0) = \frac{\langle a^\dagger a^\dagger aa \rangle}{n_p^2}, \tag{A2}$$

where applying the factorization procedure gives

$$\langle a^\dagger a^\dagger aa \rangle = n_p^2 + \delta \langle a^\dagger a^\dagger aa \rangle. \tag{A3}$$

For the doublet contribution  $\delta \langle a^\dagger a^\dagger aa \rangle$ , one repeats the steps like those leading to Eqs. (16)–(19). After some tedious algebra

$$\frac{d \delta \langle a^\dagger a^\dagger aa \rangle}{dt} = -4\gamma_c \delta \langle a^\dagger a^\dagger aa \rangle + 4g \sum_i \text{Re}(\delta \langle b^\dagger c^\dagger a^\dagger aa \rangle), \tag{A4}$$

which depends on other doublet correlations. The cluster expansion also gives the equations of motion for these correlations:

$$\begin{aligned}
\frac{d \delta \langle b^\dagger c^\dagger a^\dagger aa \rangle}{dt} &= [-(\gamma + 3\gamma_c) + i(\omega - \nu)] \delta \langle b^\dagger c^\dagger a^\dagger aa \rangle + g(n_e + n_h - 1) \delta \langle a^\dagger a^\dagger aa \rangle \\
&\quad + 2g \left[ (n_h + n_p) \delta \langle b^\dagger b a^\dagger a \rangle + (n_e + n_p) \delta \langle b^\dagger b a^\dagger a \rangle - p^2 \right],
\end{aligned} \tag{A5}$$

$$\frac{d \delta \langle c^\dagger c a^\dagger a \rangle}{dt} = -(\gamma_{nr} + 2\gamma_c) \delta \langle c^\dagger c a^\dagger a \rangle - 2g \text{Re} \left[ p(n_e + n_p) + \delta \langle b^\dagger c^\dagger a^\dagger aa \rangle \right], \tag{A6}$$

$$\frac{d \delta \langle b^\dagger b a^\dagger a \rangle}{dt} = -(\gamma_{nr} + 2\gamma_c) \delta \langle b^\dagger b a^\dagger a \rangle + 2g \text{Re} \left[ p(n_h + n_p) + \delta \langle b^\dagger c^\dagger a^\dagger aa \rangle \right], \tag{A7}$$

which must be solved simultaneously with the population and polarization equations of motion.

For the QD-QW model, it is straightforward to show that

$$\frac{d \delta \langle a^\dagger a^\dagger aa \rangle}{dt} = -4\gamma_c \delta \langle a^\dagger a^\dagger aa \rangle + 4g \sum_i n_{inh}(\omega_n) \text{Re}(\delta \langle b^\dagger; c_i a^\dagger a^\dagger a \rangle), \tag{A8}$$

$$\begin{aligned}
\frac{d \delta \langle b_i^\dagger c_i a^\dagger a^\dagger a \rangle}{dt} &= -(\gamma + 3\gamma_c) \delta \langle b_i^\dagger c_i a^\dagger a^\dagger a \rangle - 2gp_i^2 + g \left( n_{e,i}^{OD} + n_{h,i}^{OD} - 1 \right) \delta \langle a^\dagger a^\dagger aa \rangle \\
&\quad + 2g \left[ \left( n_{h,i}^{OD} + n_p \right) \delta \langle c_i^\dagger c_i a^\dagger a \rangle - \left( n_{e,i}^{OD} + n_p \right) \delta \langle b_i^\dagger b_i a^\dagger a \rangle \right],
\end{aligned} \tag{A9}$$

$$\frac{d \delta \langle c_i^\dagger c_i a^\dagger a \rangle}{dt} = -2\gamma_c \delta \langle c_i^\dagger c_i a^\dagger a \rangle - 2g \text{Re} \left[ \left( n_{e,i}^{OD} + n_p \right) p_i + \delta \langle b_i^\dagger c_i a^\dagger a^\dagger a \rangle \right], \tag{A10}$$

$$\frac{d \delta \langle b_i^\dagger b_i a^\dagger a \rangle}{dt} = -2\gamma_c \delta \langle b_i^\dagger b_i a^\dagger a \rangle + 2g \text{Re} \left[ \left( n_{h,i}^{OD} + n_p \right) p_i + \delta \langle b_i^\dagger c_i a^\dagger a^\dagger a \rangle \right]. \tag{A11}$$

The derivation for the emission linewidth is more complicated because it involves a 2-time correlation  $\langle a^\dagger(t)a(t+\tau) \rangle$ . Concerning ourselves only with the steady-state emission full-width at half maximum

$$\Delta\omega = \frac{n_p^{ss}}{2} \left[ \int_{-\infty}^{\infty} dt \left| \langle a^\dagger a(t) \rangle_{ss} \right|^2 \right]^{-1}, \tag{A12}$$

where

$$\langle a^\dagger a(t) \rangle_{ss} \equiv \lim_{t \rightarrow \infty} \langle a^\dagger(t)a(t+\tau) \rangle = G^{(1)}(\tau) e^{i\nu\tau} \tag{A13}$$



is the two-time ( $t$  and  $t + \tau$ ) laser field correlation. Removing the rapidly varying component gives  $G^{(1)}(\tau)$ . Following the steps outlined in Fig. 12, one derives the equation of motion

$$\frac{dG^{(1)}}{d\tau} = -\gamma_c G^{(1)} + 2gN_{QD}Re(S), \quad (\text{A14})$$

where

$$S(\tau) = \langle b^\dagger(\tau)c(\tau)a^\dagger \rangle_{ss} e^{i\nu\tau} \quad (\text{A15})$$

is obtained by solving

$$\frac{dS}{d\tau} = [i(\nu - \omega) - (\gamma + \gamma_c)]S + g(n_e + n_h - 1)_{ss} G^{(1)}. \quad (\text{A16})$$

- <sup>1</sup>M. O. Scully and M. S. Zubairy, *Quantum Optics* (Cambridge University Press, Cambridge, 1997).
- <sup>2</sup>L. A. Coldren, S. W. Corzine, and M. L. Masanovic, *Diode Lasers and Photonic Integrated Circuits*, 2nd ed. (Wiley, Hoboken, New Jersey, 2012).
- <sup>3</sup>S. Kreinberg, W. W. Chow, J. Wolters, C. Schneider, C. Gies, F. Jahnke, S. Hofling, M. Kamp, and S. Reitzenstein, "Emission from quantum-dot high-beta microcavities: Transition from spontaneous emission to lasing and the effects of superradiant emitter coupling," *Light: Sci. Appl.* **6**, e17030 (2017).
- <sup>4</sup>D. A. B. Miller, "Attojoule optoelectronics for low-energy information processing and communications," *J. Lightwave Technol.* **35**, 346 (2017).
- <sup>5</sup>Y. Yamamoto, S. Machida, and G. Bork, "Microcavity semiconductor lasers with enhanced spontaneous emission," *Phys. Rev.* **44**, 657 (1991).
- <sup>6</sup>K. J. Vahala, "Optical microcavities," *Nature* **424**, 839 (2003).
- <sup>7</sup>Y. Akahane, T. Asano, B.-S. Song, and S. Noda, "High-Q photonic nanocavity in a two-dimensional photonic crystal," *Nature* **425**, 944 (2003).
- <sup>8</sup>K. Petermann, "Calculated spontaneous emission factor for double-heterostructure injection lasers with gain-induced waveguiding," *IEEE J. Quantum Electron.* **15**, 566 (1979).
- <sup>9</sup>Y.-J. Lu, C.-Y. Wang, J. Kim, H.-Y. Chen, M.-Y. Lu, Y.-C. Chen, W.-H. Chang, L.-J. Chen, M. I. Stockman, C.-K. Shih, and S. Gwo, "All-color plasmonic nanolasers with ultralow thresholds: Autotuning mechanism for single-mode lasing," *Nano Lett.* **14**, 4381 (2014).
- <sup>10</sup>W. W. Chow and M. H. Crawford, "Analysis of lasers as a solution to efficiency droop in solid-state lighting," *Appl. Phys. Lett.* **107**, 141107 (2015).
- <sup>11</sup>E. Yablonovitch, "Inhibited spontaneous emission in solid-state physics and electronics," *Phys. Rev. Lett.* **58**, 2059 (1987).
- <sup>12</sup>M. Khajavikhan, A. Simic, M. Katz, J. H. Lee, B. Slutsky, A. Mizrahi, V. Lomakin, and Y. Fainman, "Thresholdless nanoscale coaxial lasers," *Nature* **482**, 204 (2012).
- <sup>13</sup>W. W. Chow, F. Jahnke, and C. Gies, "Emission properties of nanolasers during the transition to lasing," *Light: Sci. Appl.* **3**, e201 (2014).
- <sup>14</sup>A. L. Schawlow and C. H. Townes, "Infrared and optical masers," *Phys. Rev.* **112**, 1940 (1958).
- <sup>15</sup>W. H. Louisell, *Quantum Statistical Properties of Radiation* (Wiley, New York, 1990).
- <sup>16</sup>M. O. Scully and W. E. Lamb, Jr., "Quantum theory of an optical maser. I. General theory," *Phys. Rev.* **159**, 208 (1967).
- <sup>17</sup>R. Graham and H. Haken, "Quantum theory of light propagation in a fluctuating laser active medium," *Z. Phys.* **213**, 420 (1968).
- <sup>18</sup>R. Jin, D. Boggavarapu, M. Sargent III, P. Meystre, H. M. Gibbs, and G. Khitrova, "Photon-number correlations near the threshold of microcavity lasers in the weak-coupling regime," *Phys. Rev. A* **49**, 4038 (1994).
- <sup>19</sup>M. Lermer, N. Gregersen, F. Dunzer, S. Reitzenstein, and S. Hofling, "Boch-wave engineering of quantum-dot micropillars for cavity quantum electrodynamics experiments," *Phys. Rev. Lett.* **108**, 057402 (2012).
- <sup>20</sup>M. Fox, *Quantum Optics: An Introduction* (Oxford University Press, Oxford, 2006).
- <sup>21</sup>E. M. Purcell, "Spontaneous emission probabilities at radio frequencies," *Phys. Rev.* **69**, 681 (1946).
- <sup>22</sup>M. Gschrey, A. Schussler, R. Schmidt, J.-H. Schulze, T. Heindel, A. Strittmatter, and S. Reitzenstein, "In situ electron-beam lithography of deterministic single-quantum-dot mesa-structures using low-temperature cathodoluminescence spectroscopy," *Appl. Phys. Lett.* **102**, 251113 (2013).
- <sup>23</sup>S. Unsleber, Y.-M. He, S. Gerhardt, S. Maier, C.-Y. Lu, J.-W. Pan, N. Gregersen, M. Kamp, C. Schneider, and S. Hofling, "Highly indistinguishable on-demand resonance fluorescence photons from a deterministic quantum dot micropillar device with 74% extraction efficiency," *Opt. Express* **24**, 8539 (2016).
- <sup>24</sup>A. J. Shields, "Semiconductor quantum light sources," *Nat. Photonics* **1**, 215 (2007).
- <sup>25</sup>I. Aharonovich, D. Englund, and M. Toth, "Solid-state single-photon emitters," *Nat. Photonics* **10**, 631 (2016).
- <sup>26</sup>W. L. Barnes, G. Bjork, J. M. Gerard, P. Jonsson, J. A. E. Wasey, P. T. Worthing, and V. Zwiller, "Solid-state single photon sources: Light collection strategies," *Eur. Phys. J. D* **18**, 197 (2002).
- <sup>27</sup>J. H. Eberly and L. Allen, *Optical Resonances and Two-Level Atoms* (Wiley, New York, 1975).
- <sup>28</sup>A. Schlehahn, A. Thoma, P. Munnely, M. Kamp, S. Hofling, T. Heindel, C. Schneider, and S. Reitzenstein, "An electrically driven cavity-enhanced source of indistinguishable photons with 61% overall efficiency," *APL Photonics* **1**, 011301 (2016).
- <sup>29</sup>C. Gies, F. Jahnke, and W. W. Chow, "Photon antibunching from few quantum dots in a cavity," *Phys. Rev. A* **91**, 061804(R) (2015).
- <sup>30</sup>D. Meschede, H. Walther, and G. Muller, "One-atom maser," *Phys. Rev. Lett.* **54**, 551 (1985).
- <sup>31</sup>M. Nomura, N. Kumagai, S. Iwamoto, Y. Ota, and Y. Arakawa, "Photonic crystal nanocavity laser with a single quantum dot gain," *Opt. Express* **17**, 15975 (2009).
- <sup>32</sup>N. Sangouard and H. Zbinden, "What are single photons good for?," *J. Mod. Opt.* **59**, 1458 (2012).
- <sup>33</sup>A. Predojevic, M. Jezek, T. Huber, H. Jayakumar, T. Kauten, G. S. Solomon, R. Filip, and G. Weihs, "Efficiency vs. multi-photon contribution," *Opt. Express* **22**, 4789 (2014).
- <sup>34</sup>S. Ritter, P. Gartner, C. Gies, and F. Jahnke, "Emission properties and photon statistics of a single quantum dot laser," *Opt. Express* **18**, 9909 (2010).
- <sup>35</sup>E. T. Jaynes and F. W. Cummings, "Comparison of quantum and semiclassical radiation theories with application to the beam maser," *Proc. IEEE* **51**, 89 (1963).
- <sup>36</sup>M. Kira and S. W. Koch, *Semiconductor Quantum Optics* (Cambridge University Press, Cambridge, 2012).
- <sup>37</sup>W. W. Chow, S. W. Koch, and M. Sargent III, *Semiconductor-Laser Physics* (Springer, Berlin, 1993).
- <sup>38</sup>M. Sargent III, M. O. Scully, and W. E. Lamb, Jr., *Laser Physics* (Addison-Wesley, Reading, 1976).
- <sup>39</sup>M. L. Citron, H. R. Gray, C. W. Gabel, and C. R. Stroud, Jr., "Experimental study of power broadening in two-level atom," *Phys. Rev. A* **16**, 1507 (1977).
- <sup>40</sup>J. P. Reithmaier, G. Sek, A. Löffler, C. Hofmann, S. Kuhn, S. Reitzenstein, L. V. Keldysh, V. D. Kuakovskii, T. L. Reinecke, and A. Forchel, "Strong coupling in a single quantum dot-semiconductor microcavity system," *Nature* **432**, 197 (2004).
- <sup>41</sup>T. Yoshie, A. Scherer, J. Hendrickson, G. Khitrova, H. M. Gibbs, G. Rupper, C. Ell, O. B. Shchekln, and D. G. Deppe, "Vacuum Rabi splitting with a single quantum dot in a photonic crystal nanocavity," *Nature* **432**, 200 (2004).
- <sup>42</sup>K. Hennessy, A. Badolato, M. Winger, D. Gerace, M. Atature, S. Gulde, S. Falt, E. L. Hu, and A. Imamoglu, "Quantum nature of a strongly coupled single quantum dot-cavity system," *Nature* **445**, 896 (2007).
- <sup>43</sup>C. Gies, F. Gericke, P. Gartner, S. Holzinger, C. Hopfmann, T. Heindel, J. Wolters, C. Schneider, M. Florian, F. Jahnke, S. Hofling, M. Kamp, and S. Reitzenstein, "Strong light-matter coupling in the presence of lasing," *Phys. Rev. A* **96**, 023806 (2017).
- <sup>44</sup>H. Leymann, A. Foerster, F. Jahnke, J. Wiersig, and C. Gies, "Sub- and superradiant emission in nanolasers," *Phys. Rev. Appl.* **4**, 044018 (2015).
- <sup>45</sup>E. Gibney, "Nobel for blue LED that revolutionized lighting," *Nature* **514**, 152 (2014).
- <sup>46</sup>M. R. Krames, O. B. Shchekin, R. Mueller-Mach, G. O. Mueller, L. Zhou, G. Harbers, and M. G. Craford, "Status and future of high-power light-emitting diodes for solid-state lighting," *J. Disp. Technol.* **3**, 160 (2007).
- <sup>47</sup>A. Bykhovshi, B. Gelmonst, and M. Shur, "The influence of the strain-induced electric field on the charge distribution in GaN-AlN-GaN structure," *J. Appl. Phys.* **74**, 6734 (1993).
- <sup>48</sup>H. Soda, K. Iga, C. Kitahara, and Y. Suematsu, "GaInAsP/InP surface emitting injection lasers," *Jpn. J. Appl. Phys., Part 1* **18**, 2329 (1979).

- <sup>49</sup>H. M. Gibbs, S. L. McCall, T. N. C. Venkatesan, A. C. Gossard, A. Passner, and W. Wiegmann, "Optical bistability in semiconductors," *Appl. Phys. Lett.* **35**, 451 (1979).
- <sup>50</sup>F. Koyama, S. Kinoshita, and K. Iga, "Room-temperature continuous wave lasing characteristics of GaAs vertical cavity surface-emitting laser," *Appl. Phys. Lett.* **55**, 221 (1989).
- <sup>51</sup>J. L. Jewell, A. Scherer, S. L. McCall, Y. H. Lee, S. Walker, J. P. Harbison, and L. T. Florez, "Low-threshold electrically pumped vertical-cavity surface-emitting microlasers," *Electron. Lett.* **25**, 1123 (1989).
- <sup>52</sup>K. L. Lear, R. P. Schneider, Jr., K. D. Choquette, S. P. Kilcoyne, and K. M. Geib, "Selectively oxidised vertical cavity surface emitting lasers with 50% power conversion efficiency," *Electron. Lett.* **31**, 208 (1995).
- <sup>53</sup>D. Thomson, A. Zilkie, J. E. Bowers, T. Komljenovic, G. T. Reed, L. Vivien, D. Marris-Morini, E. Cassan, L. Viot, and J.-M. Fedeli, "Roadmap on silicon photonics," *J. Opt.* **18**, 073003 (2016).
- <sup>54</sup>W. W. Chow, A. Y. Liu, A. C. Gossard, and J. E. Bowers, "Extraction of inhomogeneous broadening and nonradiative losses in InAs quantum-dot lasers," *Appl. Phys. Lett.* **107**, 171106 (2015).
- <sup>55</sup>H. Carmichael, *An Open Systems Approach to Quantum Optics* (Springer Verlag, Berlin, 1991).
- <sup>56</sup>W. W. Chow and F. Jahnke, "On the physics of semiconductor quantum dots for applications in lasers and quantum optics," *Prog. Quantum Electron.* **37**, 109 (2013).